High Spectral Resolution Lidar – generation 2 (HSRL-2) Retrievals of Ocean Surface Wind Speed: Methodology and Evaluation

Sanja Dmitrovic[1], Johnathan W. Hair[2], Brian L. Collister[2], Ewan Crosbie[2,3], Marta A. Fenn[2], Richard A. Ferrare[2], David B. Harper[2], Chris A. Hostetler[2], Yongxiang Hu[2], John A. Reagan[4], Claire E. Robinson[2,3,+], Shane T. Seaman[2], Taylor J. Shingler[2], Kenneth L. Thornhill[2,3], Holger Vömel[5], Xubin Zeng[6], Armin Sorooshian[1,6,7]

[1]James C. Wyant College of Optical Sciences, University of Arizona, Tucson, AZ 85721, USA
[2]NASA Langley Research Center, Hampton, VA 23681, USA
[3]Analytical Mechanics Associates, Hampton, VA 23666, USA
[4]Department of Electrical and Computer Engineering, University of Arizona, Tucson, AZ 85721, USA
[5]National Center for Atmospheric Research, Boulder, CO 80307, USA
[6]Department of Hydrology and Atmospheric Sciences, University of Arizona, Tucson, AZ 85721, USA
[7]Department of Chemical and Environmental Engineering, University of Arizona, Tucson, AZ 85721, USA
[+]Deceased

Correspondence to: Armin Sorooshian (armin@arizona.edu)

Abstract. Ocean surface wind speed (i.e., wind speed 10 m above sea level) is a critical parameter used by atmospheric models to estimate the state of the marine atmospheric boundary layer (MABL). Accurate surface wind speed measurements in diverse locations are required to improve characterization of MABL dynamics and assess how models simulate large-scale phenomena related to climate change and global weather patterns. To provide these measurements, this study introduces and evaluates a new surface wind speed data product from NASA Langley Research Center's High Spectral Resolution Lidar – generation 2 (HSRL-2) using data collected as part of NASA's Aerosol Cloud meTeorology Interactions oVer the western ATlantic Experiment (ACTIVATE) mission. The HSRL-2 can directly measure vertically resolved aerosol backscatter and extinction profiles without additional constraints or assumptions, enabling the instrument to accurately derive atmospheric attenuation and directly determine surface reflectance (i.e., surface backscatter). Also, the high horizontal spatial resolution of the HSRL-2 retrievals (0.5 s or ~75 m along track) allows the instrument to probe the fine-scale spatial variability of surface wind speeds over time along the flight track and breaks in broken cloud fields. A rigorous evaluation on these retrievals is performed by comparing coincident HSRL-2 and National Center for Atmospheric Research (NCAR) AVAPS dropsonde data, owing to the joint deployment of these two instruments on ACTIVATE's King Air aircraft. These comparisons show correlations of 0.89, slopes of 1.04 and 1.17, and y-intercepts of -0.13 m s^{-1} and -1.05 m s^{-1} for linear and bisector regressions, respectively and the overall accuracy is calculated to be 0.15 m s^{-1} ± 1.80 m s^{-1}. It is also shown that the dropsonde surface wind speed data most closely follows the HSRL-2 distribution of wave-slope variance using the distribution proposed by Hu et al. (2008) than the ones proposed by Cox and Munk (1954) and Wu (1990) for surface wind speeds below 7 m s^{-1}, with this category comprising most of the ACTIVATE data set. The retrievals are then evaluated separately for surface wind speeds below 7 m s^{-1} and between 7 m s^{-1} and 13.3 m s^{-1} and show that the HSRL-2 retrieves surface wind speeds with a bias of ~0.5 m s^{-1} and an error of ~1.5 m s^{-1}, a finding not apparent in the cumulative comparisons. Also, it is shown that the HSRL-2 retrievals are more

Style Definition: EndNote Bibliography: Line spacing: 1.5 lines

Formatted: Space Before: 6 pt

accurate in the summer (-0.18 m s^{-1} ± 1.52 m s^{-1}) than winter (0.63 m s^{-1} ± 2.07 m s^{-1}), but the HSRL-2 is still able to make numerous, (N = 236) accurate retrievals in the winter. Overall, this study highlights the abilities and assesses the performance of the HSRL-2 surface wind speed retrievals and it is hoped that further evaluation of these retrievals will be performed using other airborne and satellite data sets. **Abstract.** This study introduces and evaluates ocean surface wind speed retrieval capabilities of the High Spectral Resolution Lidar – generation 2 (HSRL-2) instrument through comparison with wind speed data collected by National Center for Atmospheric Research (NCAR) Airborne Vertical Atmospheric Profiling System (AVAPS) dropsondes. Wind speed is derived from HSRL-2 measurements of the transmitted laser's specular reflection off the ocean surface. The magnitude of the surface reflectivity is determined by the surface's wave-slope variance, which is driven by surface winds. The assessment relies on the multi-year airborne data set collected as part of NASA's Aerosol Cloud meTeorology Interactions oVer the western ATlantic Experiment (ACTIVATE) campaign, where HSRL-2 retrievals and AVAPS dropsonde measurements of surface wind speeds were horizontally synchronized owing to their joint deployment on one of two aircraft used during the mission. A total of 577 collocated HSRL-2 – dropsonde surface wind speed data points over the northwest Atlantic Ocean are used for this study. Treating the dropsonde wind speeds as truth, it is found that, through two established wind speed – wave-slope parameterizations, the HSRL-2 wind speed retrievals have small errors (0.15 m s^{-1} ± 1.80 m s^{-1} and 0.62 m s^{-1} ± 1.70 m s^{-1}) and high correlation coefficients (0.89 and 0.88) with dropsonde wind speed measurements. Also, HSRL-2 wind speed error is higher in winter than in summer due at least partly to the higher frequency of low wind speeds and reduced cloud fraction in summer. Two research flights from 28 August 2020 and 1 March 2020 serve as detailed case studies to show the success of the collocation method based on ACTIVATE's spatial coordination strategy and how HSRL-2 wind speed retrievals can enhance science-oriented studies such as those related to cloud evolution and general air-sea interaction. Another case flight examined from 11 January 2022 demonstrates the challenge of conducting HSRL-2 wind speed retrievals in high cloud fraction conditions. Overall, this study highlights the airborne HSRL-2's ability to retrieve surface wind speeds with accuracy as well as the potential of using dropsondes to validate aircraft instrument data sets within a field campaign.

Formatted: Font color: Black

1 Introduction

The layer between the ocean and free troposphere, known as the marine atmospheric boundary layer (MABL), hosts is the target of various types of research because of the host of processes that occur, such as the modulation of sensible and latent heat fluxes, the exchange of gases such as carbon dioxide, thecloud evolution of clouds, and the transport of aerosol particles (Neukermans et al., 2018). Improved characterization of MABL dynamics is required to accurately simulate large-scale phenomena related tosuch as climate change and global weather patterns (Paiva et al., 2021). This characterization relies on a combination of global numerical weather prediction (NWP) models and real observations (Carvalho, 2019). One of the most influential parameters that driveTo model these MABL processes is dynamics and associated phenomena, ocean surface wind speeds or wind speeds at 10 m above sea level (hereafter calledare needed. Although not the lone governing factor, surface

wind speeds). Therefore, instruments such as lidar are used to provide accurate surface wind speed measurements in various geographical locations to improve estimations of the MABL state globally. For instance, satellite ~~are a critical parameter for modelling sea salt aerosol emissions from the ocean surface (Reid et al., 2001) and in studies of cloud microphysics (Colón-Robles et al., 2006) since these winds directly lead to increases in sea salt particle concentrations and activation of these particles that turn them into cloud condensation nuclei (CCN).~~

~~Although~~ lidar systems that measure aerosol and cloud vertical distributions, ~~onboard platforms~~ such as the lidar on board the NASA Cloud-Aerosol Lidar and Infrared Pathfinder Observation (CALIPSO) satellite~~, have been deployed to measure aerosol and cloud vertical distributions, they~~ also have the capability to provide horizontally-resolved surface wind speed data. ~~(Hu et al., 2008).~~ The underlying principle of lidar surface~~the CALIPSO~~ wind speed retrievals was first derived by ~~from the theory of~~ Cox and Munk (1954)~~, (referred to as CM54 hereafter),~~ where bidirectional reflectance measurements of sea-surface glint are used to establish a Gaussian relationship between ~~ocean~~ surface wind speeds and the distribution of wind-driven wave slopes. To probe these surface wave slopes, lidar instruments emit~~CALIPSO emitted~~ laser pulses into the atmosphere and measure~~measured~~ the reflectance (or backscatter) of those laser pulses from particles, molecules, and the ocean surface. The magnitude of the measured signal is then ~~ocean surface reflectance was~~ used to estimate the variance of the wave- slope distribution (i.e., ~~wave slope variance). The wind speed (U) was then approximated from the~~ wave-slope variance) and therefore surface wind speed. Note that reflectance and backscatter are used interchangeably throughout ~~(σ^2) through~~ this paper.

~~linear relationship:~~

$$U = \left(\frac{(\sigma^2) - 3.0E - 3}{5.12E - 3}\right). \quad (1)$$

~~Although CALIPSO retrievals of surface wind speeds~~ Although many studies have expanded upon the original Cox-Munk relationship (e.g., Hu et al., 2008; Josset et al., 2008; Josset et al., 2010a; Kiliyanpilakkil and Meskhidze, 2011; Nair and Rajeev, 2014; Murphy and Hu, 2021; Sun et al., 2023), these parameterizations do not account for atmospheric attenuation by aerosols and therefore have difficulty in calibrating~~been used in many studies (e.g., Hu et al., 2008; Josset et al., 2010a; Josset et al., 2010b; Kiliyanpilakkil and Meskhidze, 2011; Nair and Rajeev, 2014; Murphy and Hu, 2021; Sun et al., 2023), the main drawback is that one must have an accurate calibration of~~ the measured ocean surface reflectance accurately. This presents a difficulty for elastic backscatter lidars like CALIPSO, for which the signal is typically calibrated high in the atmosphere where molecular backscatter dominates and aerosol backscatter is insignificant or can be accurately estimated. The problem lies in the transfer of this calibration to the ocean surface, which entails accounting for the attenuation of the transmitted and backscattered light by the intervening atmosphere between the calibration region and the ocean surface. If coincident aerosol optical depth (AOD) data are available (e.g., from MODIS in the case of CALIPSO detailed in Josset et al. (2008))~~)~~ then they~~those AOD data~~ may be used to estimate the intervening attenuation and transfer the calibration. However, such data from

passive sensors including MODIS are only available during daytime, ~~and even then~~ are typically not produced in the vicinity of clouds and may have unacceptably high uncertainties for accurately accounting for aerosol attenuation.~~.~~ Estimation of the attenuation from the lidar data alone requires an assumption of the aerosol extinction-to-backscatter ratio (or "lidar ratio"), so errors in the assumed value can lead to an incorrect~~create significant errors in the~~ estimate of attenuation, especially when AOD is high. Because of this, the surface ~~surface~~ wind speed estimates in Hu et al. (2008)~~Hu et al. (2008)~~ were limited to scenes with no clouds and negligible aerosol loading~~very low AODs~~.

This study addresses retrieving surface ~~surface~~ wind speed directly from a lidar without other assumptions or external constraints by employing the high-spectral-resolution lidar (HSRL) technique through NASA Langley Research Center's (LaRC's) airborne High Spectral Resolution Lidar – generation 2 (HSRL-2) instrument (Hair et al., 2008~~; Burton et al, 2018~~). The HSRL-2 can directly measure vertically resolved aerosol backscatter and extinction profiles without relying on an assumed lidar ratio or other external aerosol constraints, enabling accurate estimates of the attenuation of the atmosphere. Therefore, the surface reflectance can be directly determined, providing a measure of the wave-slope variance and thus surface wind speed. ~~This paper focuses on a new ocean surface wind speed product leveraging this instrument's capabilities.~~ This study details the HSRL-2's ~~ocean~~ surface wind speed retrieval methodology and evaluates this~~the aforementioned~~ surface wind speed product through comparison with measurements from National Center for Atmospheric Research (NCAR) Airborne Vertical Atmospheric Profiling System (AVAPS) dropsondes. This work leverages an extensive data set from NASA's Aerosol Cloud meTeorology Interactions oVer the western ATlantic Experiment (ACTIVATE) mission, which had multiple scientific and technological objectives described in Sect. 2.1~~detail elsewhere~~ (Sorooshian et al., 2019). The mission consisted of six deployments between 2020 and 2022 and featured the joint deployment of the HSRL-2 and dropsonde launcher on one of its two aircraft to enable~~enabling~~ direct comparison~~intercomparison~~ between the two instrument data sets. The~~ACTIVATE data across its six deployments between 2020 and 2022 are specifically examined. Section 2 provides a detailed description of the HSRL-2 wind speed retrieval algorithm, the ACTIVATE~~ mission, ~~the NCAR AVAPS~~ dropsonde ~~system, data collocation procedures, and how statistical analysis on the data is performed. This section also showcases a research flight from 28 August 2020 to demonstrate the success of ACTIVATE's spatially coordinated flight approach. Section 3 summarizes results of both cumulative wind speed intercomparisons for ACTIVATE's multi-year data set~~ and HSRL-2 instrumentation,~~two additional case study flights highlighting 1) the ability of the~~ HSRL-2 algorithm, ~~to provide continuous surface wind speed profiles that enable the study of cloud evolution~~ and the methods~~sea-surface temperature dynamics~~ and results~~2) the potential drawback~~ of using/evaluating the HSRL-2 ~~this wind speed product on days with high cloud fraction conditions. Section 4 presents conclusions discussing the success~~ and dropsonde surface wind speed data sets are all detailed in the following discussion. ~~limitations of this methodology as well as motivating future studies utilizing aircraft and satellite wind speed data.~~

2 Methods

2.1 ACTIVATE Mission Description~~2.1 HSRL-2 Wind Speed Retrieval Method~~

The HSRL-2 ocean surface wind speed product is assessed during the ACTIVATE campaign, which is a NASA Earth Venture Suborbital-3 (EVS-3) mission.~~The NASA LaRC HSRL-2 is a lidar instrument designed for airborne operation with the capability to obtain vertically resolved aerosol properties such as aerosol backscatter and depolarization at three wavelengths (355, 532, 1064 nm) along with aerosol extinction at two wavelengths (355 and 532 nm) (Hair et al., 2008; Burton et al., 2018). In addition to these aerosol products, several new geophysical products have (and continue to be) developed, including an aerosol classification routine (Burton et al. 2012), retrievals of atmospheric mixed layer height (Scarino et al., 2014), ocean subsurface particulate backscatter and attenuation coefficients (Schulien et al., 2017), cloud optical properties (in development), and the focus of this study, 10-m surface wind speeds. The retrieval method is described in detail below.~~

The primary aim of ACTIVATE is to improve knowledge of aerosol-cloud-meteorology interactions, which are linked to the highest uncertainty among components contributing to total anthropogenic radiative forcing (Bellouin et al., 2020). There are three major scientific objectives: (i) characterize interrelationships between aerosol particle number concentration (N_a), CCN concentration, and cloud drop number concentration (N_d) with the goal of decreasing uncertainty in model parameterizations of droplet activation; (ii) advance process-level knowledge and simulation of cloud microphysical and macrophysical properties, including the coupling of aerosol effects on clouds and cloud effects on aerosol particles; and (iii) assess remote sensing capabilities to retrieve geophysical variables related to aerosol-cloud interactions. This study focuses on the third objective, which has already received attention with ACTIVATE data for retrievals other than ocean surface wind speeds (Schlosser et al., 2022; Van Diedenhoven et al., 2022; Chemyakin et al., 2023; Ferrare et al., 2023). ACTIVATE built a high volume of flight data statistics over the Western North Atlantic Ocean (WNAO) by flying six deployments across three years (2020 – 2022), with a winter and summer deployment each year (Sorooshian et al., 2023). Winter deployments included the following date ranges: 14 February – 12 March (2020), 27 January – 2 April (2021), 30 November 2021 – 29 March (2022). Summer deployments were as follows: 13 August – 30 September (2020), 13 May – 30 June (2021), 3 May – 18 June (2022). Across all three years, 90 King Air flights during the winter deployment were performed with 373 dropsondes launched while 78 flights during the summer deployment took place with 412 dropsondes launched.

Two NASA Langley aircraft flew in spatial and temporal coordination for the majority of the total flights (162 of 179). A "stacked" flight strategy was developed where a low-flying (< 5 km) HU-25 aircraft collected in situ data in and just above the MABL while a high-flying (~9 km) King Air aircraft simultaneously provided remote sensing retrievals and dropsonde measurements in the same altitude range. In doing so, the stacked aircraft would simultaneously obtain data relevant to aerosol-cloud-meteorology interactions in the same column of the atmosphere and provide a complete picture of the lower troposphere (Sorooshian et al., 2019). In situ measurements of gases, particles, meteorological variables, and cloud properties were

Field Code Changed

Field Code Changed

conducted by the HU-25 Falcon. The King Air's payload included the NASA Goddard Institute for Space Studies (GISS) Research Scanning Polarimeter (RSP) and the two instruments relevant to this work: the NASA LaRC HSRL-2 and the NCAR AVAPS dropsondes (Sorooshian et al., 2023). An advantage of the joint deployment of HSRL-2 and AVAPS dropsondes on the King Air is that the data are spatially synchronized at launch, with wind drift of the dropsondes during descent accounted for with procedures summarized in Sect. 2.3.

The rationale to fly over the WNAO in different seasons was to collect data across a wide range of aerosol and meteorological regimes, with the latter promoting a broad range of cloud conditions (Painemal et al., 2021). A significant meteorological feature is the North Atlantic Oscillation, which is the oscillation between the Bermuda-Azores High (high pressure system) and the Icelandic Low (low pressure system) (Lamb and Peppler, 1987). In the summer, the Bermuda-Azores High is at its peak and introduces easterly and southwesterly trade winds (Sorooshian et al., 2020). Starting in the fall, the Icelandic Low becomes prominent and introduces westerly winds in the boundary layer. The balancing act between these pressure systems dictates the climate of the North Atlantic and the prevailing transport processes (Li et al., 2002; Creilson et al., 2003; Christoudias et al., 2012). These transport processes that vary seasonally explain why winter flights coincided with more offshore (westerly) flow containing aerosol types impacted by anthropogenic influence (e.g., Corral et al., 2022), whereas summer flights included more influence from wildfire emissions and African dust among other sources both natural and anthropogenic in nature (Mardi et al., 2021; Aldhaif et al., 2020). Winds and turbulence tend to be stronger in the winter due to higher temperature gradients between the air and the ocean (Brunke et al., 2022), resulting in a higher fraction of available aerosol particles in the MABL that activate into cloud droplets in winter coinciding with cold air outbreaks as compared to summer (Dadashazar et al., 2021; Kirschler et al., 2022; Painemal et al., 2023). Therefore, this study region allows the HSRL-2 surface wind speed retrievals to be evaluated in various meteorological and aerosol loading conditions.

Field Code Changed

2.2 Dropsondes

The AVAPS system deployed during the ACTIVATE mission utilized the newer, more reliable NRD41 mini sondes. Their smaller form factor along with updates to their launching hardware increased reliability for launches since these instruments could be used with more aircraft and launcher configurations (Vömel and Dunion, 2023). A variable number of dropsondes were launched per flight, usually 3 to 4 for routine flights, with more being launched for specific targeted flight opportunities. With response times much less than 1 second, AVAPS samples position, wind speed (with 0.5 m s^{-1} uncertainty) (Vömel and Dunion, 2023), and state variables such as pressure, temperature, and humidity all the way to ~6 m above the ocean surface. The data are then post-processed via NCAR's Atmospheric Sounding Processing Environment (ASPEN) software where any spurious data are removed including any data returned from the ocean surface itself (Martin and Suhr, 2021). More details on the AVAPS system and its usage on other aircraft and missions can be found in (Vömel et al., 2021) and details of its usage in ACTIVATE specifically can be found in Vömel and Dunion (2023). Not many studies exist on surface wind speed validation

of aircraft instruments with dropsondes (Bedka et al., 2021), so this study also highlights the potential of using dropsondes to validate aircraft surface wind speed data.

2.3 HSRL-2 Instrument Description

The NASA LaRC HSRL-2 is an airborne lidar instrument designed to enable vertically resolved retrievals of aerosol properties such as aerosol backscatter and depolarization at three wavelengths (355, 532, and 1064 nm), aerosol extinction at two wavelengths (355 and 532 nm) (Hair et al., 2008; Burton et al., 2018), and aerosol classification (Burton et al., 2012). In addition to these aerosol products, other retrieval capabilities include retrievals of atmospheric mixed layer height (Scarino et al., 2014), ocean subsurface particulate backscatter and attenuation coefficients (Schulien et al., 2017), cloud optical properties (in development), and 10 m surface wind speeds, the latter of which is the focus of this study. Details of the laser receiver optics and detectors are described in detail in Hair et al. (2008). This analysis utilizes the 532 nm data channels that include a total scattering channel (both molecular and particulate scattering), molecular scattering only, and the cross polarized channel, which are internally calibrated during flight. Key to determining the optical transmission and subsurface signals is a molecular channel that filters essentially all the particulate and specular scattering using the iodine notch filter as described in Hair et al. (2008), determining both the laser transmission down to the surface and correction of the subsurface scattering contribution to the integrated surface backscatter signal. The lidar is operated in a nadir-only viewing geometry (i.e., not scanning). The laser is a custom built 200 Hz repetition rate Nd:YAG laser emitting at 1064 nm, which is converted to both the second and third harmonic wavelengths of 532 nm and 355 nm, respectively. The output laser energies are nominally 34 mJ (1064 nm), 11 mJ (532 and 355 nm each) and each is set to a divergence ($1/e^2$) of approximately 0.8 mrad, giving a beam footprint diameter on the ocean surface of ~7 m for the nominal 9 km King Air flight altitude. The telescope is set to a full field of view of 1 mrad, giving a viewing footprint diameter of 9 m at the ocean surface at nominal flight altitude. All three wavelengths are transmitted coaxially with the telescope through a fused silica window in the bottom of the aircraft are actively boresighted to the receiver. The HSRL-2 incorporates high speed photomultiplier tubes (PMTs) and custom amplifiers to allow data collection at 120 MHz sampling rates with 40 MHz bandwidths. Data are sampled at 120 MHz (1.25 m in the atmosphere and 0.94 m in the ocean) with 16-bit digitizers and single-shot profiles are summed over 100 laser shots during 0.5 s which is the fundamental acquisition interval before storing to a disk. The aircraft incorporates an Applanix Inertial Navigation System (INS) to record the aircraft altitude at 0.5 s time intervals corresponding to each 100-shot data profile. For the surface wind speed calculations, data are screened to limit the pitch and roll to less than +/- 3° from the median values, which are approximately 0° for the roll and 3° - 5° for pitch on the King Air.

2.4 HSRL-2 Surface Wind Speed Retrieval Method

As mentioned in the previous section~~Sect. 1~~, a lidar system emits laser pulses into the atmosphere and the backscattered light from particles (aerosols) and molecules is collected with a telescope and imaged onto optical detectors where the generated

analog electrical signal is digitally sampled as a function of time. Backscatter is also received from the reflection of the laser pulse off the ocean surface and is referred to as the "surface return" signal. To derive surface wind speeds, the surface backscattered (180°) reflected radiance~~backscatter~~ (β_{surf} , units sr^{-1}) is estimated from the surface return signal and related to the wave-slope variance (σ^2), as detailed in Josset et al. (2010b), through

$$\beta_{surf} = \frac{C_F}{4\pi\sigma^2 cos^5(\theta)} e^{-\frac{tan^2(\theta)}{\sigma^2}}, \quad (2)$$

where C_F is the Fresnel coefficient and is set to 0.0205 as given in Venkata and Reagan (2016) and θ is the angle of incidence of the laser with the ocean surface. The calculations are made only when the pitch and roll of the aircraft vary less than 3° from the median values to limit conditions where the aircraft altitude changes rapidly within the 0.5 s data collection window. The mean wind speed at 10 m above the sea surface (U) is then derived using a piecewise empirical relationship between surface wind speed and wave-slope variance from Hu et al. (2008), where:~~where C_F is the Fresnel coefficient and θ is the omnidirectional nadir offset angle. The mean wind speed at 10 m above the sea surface (U) is then derived using a piecewise empirical relationship between wind speed and wave-slope variance from Hu et al. (2008) (referred to as Hu08 hereafter), where:~~

$$U = \left(\frac{\langle\sigma^2\rangle}{0.0146}\right)^2, \langle\sigma^2\rangle < 0.0386, U < 7\ m\ s^{-1}, \quad (3.1)$$

$$U = \left(\frac{\langle\sigma^2\rangle - 3.0E{-}3}{5.12E{-}3}\right), 0.0386 \leq \langle\sigma^2\rangle < 0.0711,\ 7\ m\ s^{-1} \leq U < 13.3\ m\ s^{-1}, \quad (3.2)$$

$$U = 10^{\left(\frac{\langle\sigma^2\rangle + 0.084}{0.138}\right)}, \langle\sigma^2\rangle \geq 0.0711, U \geq 13.3\ m\ s^{-1}. \quad (3.3)$$

The relationships shown in Eqs. 3.1 – 3.3 were derived by Hu et al. (2008) using the comparisons between AMSR-E surface wind speeds and CALIPSO backscatter reflectance mentioned in Sect. 1 and agree identically with the Cox-Munk relationship for surface wind speeds between 7 m s^{-1} and 13.3 m s^{-1} and the log-linear relationship proposed by Wu (1990) for surface wind speeds above 13.3 m s^{-1}. ~~The relationships shown in Eqs. 3.1 – 3.3 were established by Hu08 using the comparisons between AMSR-E wind speeds and CALIPSO backscatter reflectance mentioned in Sect. 1. Note that Eq. 3.2 is similar to the linear relationship proposed by CM54 (Eq. 1) and Eq. 3.3 is similar to the log-linear relationship proposed by Wu (1990). Although there are other relationships that have been provided in the literature such as Venkata and Reagan (2016), the Hu08 relationship is focused on to be consistent with CALIPSO retrievals. Summary statistics are also shown using the CM54 relationship, which is widely applied in current remote sensing retrievals.~~

With respect to ~~surface~~ surface wind speed retrievals, the HSRL-2 instrument offers two major advantages over standard backscatter lidars such as CALIPSO: 1) it can account for atmospheric attenuation between the aircraft and the surface so retrievals can be performed without constraining the retrieval to low AOD~~optical depth~~ conditions (i.e., negligible aerosol loading) or assuming the lidar ratio, and 2) it has high vertical resolution sampling (1.25 m) that enables accurate correction

for ocean subsurface scattering, which makes a small but non-negligible contribution to the measured surface return. The equations for the HSRL-2 532-nm measurement channels are:

$$P_{mol}(r) = G_{mol}\frac{1}{r^2}F(r)\beta_m^{\parallel}(r)T^2(r), \tag{4.1}$$

$$P_{tot}(r) = G_{mol}G_{i2}\frac{1}{r^2}\left[\left(\beta_p^{\parallel}(r)+\beta_m^{\parallel}(r)\right)+G_{dep}\left(\beta_p^{\perp}(r)+\beta_m^{\perp}(r)\right)\right]T^2(r) \tag{4.2}$$

where P_x is the total measured signal per sampling interval by the lidar and r denotes the range from the lidar. Here the *mol* subscript denotes the measured signal on the molecular channel, for which all particulate backscatter and the surface return is blocked by an iodine vapor filter. The *tot* subscript denotes the "total" backscatter calculated from the sum of two measurement channels, the co-polarized channel and the cross-polarized channel. These channels are essentially elastic backscatter lidar channels similar to the 532 ~~-~~nm channels on CALIPSO, in that they measure attenuated backscatter from both molecules and particles. The co-polarized channel measures backscatter that is polarized parallel to the linear polarization of the transmitted laser pulses, and the cross-polarized channel measures backscatter with polarization perpendicular to the laser pulses. The volume backscatter coefficient, β (units m^{-1} sr^{-1}), is separated~~broken out~~ into components arising from either molecular scattering (*m*) or particulate scattering (*p*) and by polarization parallel (∥) and perpendicular (⊥) to the laser. The combined collection efficiency, optical efficiency, and the overall electronic gain for the signals is denoted by G_x. The T^2 factor is the two-way transmission of the atmosphere, which accounts for both molecular and particulate scattering and absorption between the lidar and range r. A full description of the instrument channels are~~is~~ described in Hair et al. (2008).

Eqs. 4.1 and 4.2 are generalized such that the backscatter coefficients and transmission factors can be either from the atmosphere or ocean, depending on the altitude (or depth) of the scattering volume. Also, the transmission of the molecular backscatter through the iodine vapor filter, *F*, is based on either the atmosphere (*atm*) or the ocean (*ocn*) scattering regions, as they have different backscatter spectra and thus different iodine filter transmission factors, both of which are determined by laboratory calibrations and ~~the~~ modeled molecular scattering spectra (Hair et al., 2008~~; Hair et al., 2016~~). Calibration operations are conducted during each flight to provide the relative gain ratios between the molecular (*mol*) and co-polarized (*par*) channels, G_{i2}, and between the co-polarized and cross-polarized (*per*) channels, G_{dep}, such that

$$G_{i2} = \frac{G_{par}}{G_{mol}},\ G_{dep} = \frac{G_{per}}{G_{par}}. \tag{5}$$

After the internal gain ratios (Eq. 5) are applied, the two signals (Eqs. 4.1 and 4.2) have the same relative gain~~, such that the magnitude of P_{mol} is equal to the magnitude of co-polarized molecular component of P_{tot}~~. As will be shown below, the retrieval implements ratios of these two signals, and therefore neither the absolute gain nor any other absolute calibration factor is required to determine the surface backscatter.

To calculate the surface backscatter, the overall system response must be accounted for. The measured signal (P) is the convolution of the normalized system response, (L), with the ideal measured signal (i.e., infinite detection bandwidth and delta-

function-like laser pulse), this signal being the gain-scaled (G), range-scaled ($\frac{1}{r^2}$), attenuated (T^2) backscatter coefficient (β, units $m^{-1}sr^{-1}$), which can be written as

$$P_{ideal}(r) = G\frac{1}{r^2}\,\beta(r)\,T^2(r). \tag{6a}$$

$$P(r) = G\int_{-\infty}^{\infty} L(r-\rho)\,P_{ideal}(\rho)\,d\rho. \tag{6b}$$

The system response includes the impact of the laser's temporal pulse shape, detector response, and analog electronic filter response.

To account for different scattering media and to better understand how the system response impacts the surface backscatter calculation, it is helpful to separate the total scattering channel, $P_{tot}(r)$, into three contributions: atmosphere [atm], surface [$surf$], and ocean [ocn] as follows:

$$P_{tot}(r) = P_{tot}^{atm}(r) + P_{tot}^{ocn}(r) + P_{tot}^{surf}(r). \tag{7}$$

Using Eq. 6, the last term in Eq. 7, $P_{tot}^{surf}(r)$, can be written as

$$P_{tot}^{surf}(r) = G_{mol}G_{i2}\int_{-\infty}^{\infty} L(r-\rho)\frac{1}{\rho^2}\beta_{surf}\delta(\rho-r_s)T^2(\rho)d\rho \tag{8a}$$

$$P_{tot}^{surf}(r) = G_{mol}G_{i2}L(r-r_s)\frac{1}{r_s^2}\beta_{surf}T^2(r_s) \tag{8b}$$

where the range to the ocean surface is r_s and the volume backscatter coefficient for the ocean surface is represented as $\beta_{surf}\delta(\rho-r_s)$ (units m^{-1} sr^{-1}), where $\delta(\rho-r_s)$ is the Dirac delta function centered at r_s. Figure 1 illustrates the vertical distributions of the measured~~The measurement~~ signals P_{tot} (black) and P_{mol} (blue) along with the P_{tot}^{surf} (green) component of P_{tot}. Note that zero altitude is the location of the ocean surface.~~as detailed in Eqs. 6—8 are then visualized in Fig. 1.~~

Formatted Table

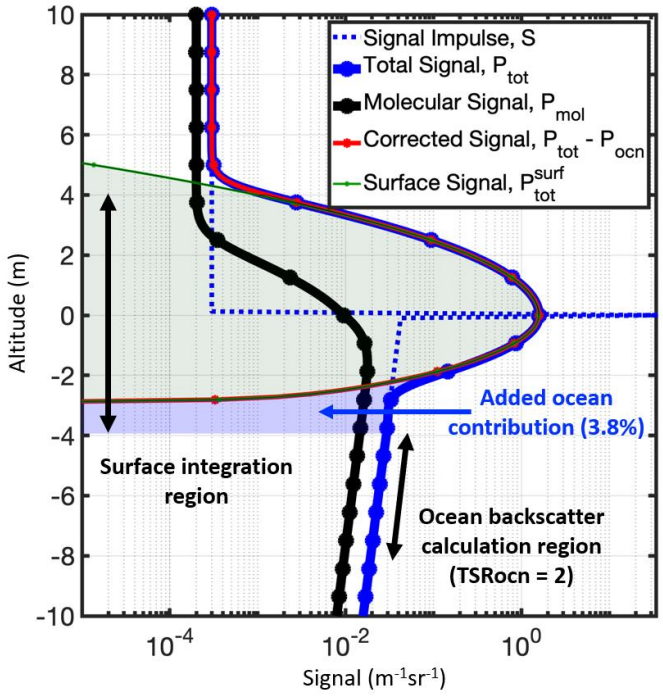
Signal Impulse, S
Total Signal, P_{tot}
Molecular Signal, P_{mol}
Corrected Signal, P_{tot} - P_{ocn}
Surface Signal, P_{tot}^{surf}
Added ocean contribution (3.8%)
Surface integration region
Ocean backscatter calculation region (TSRocn = 2)
Altitude (m)
Signal ($m^{-1}sr^{-1}$)
10
8
6
4
2
0
-2
-4
-6
-8
-10
10^{-4}
10^{-2}
10^{0}

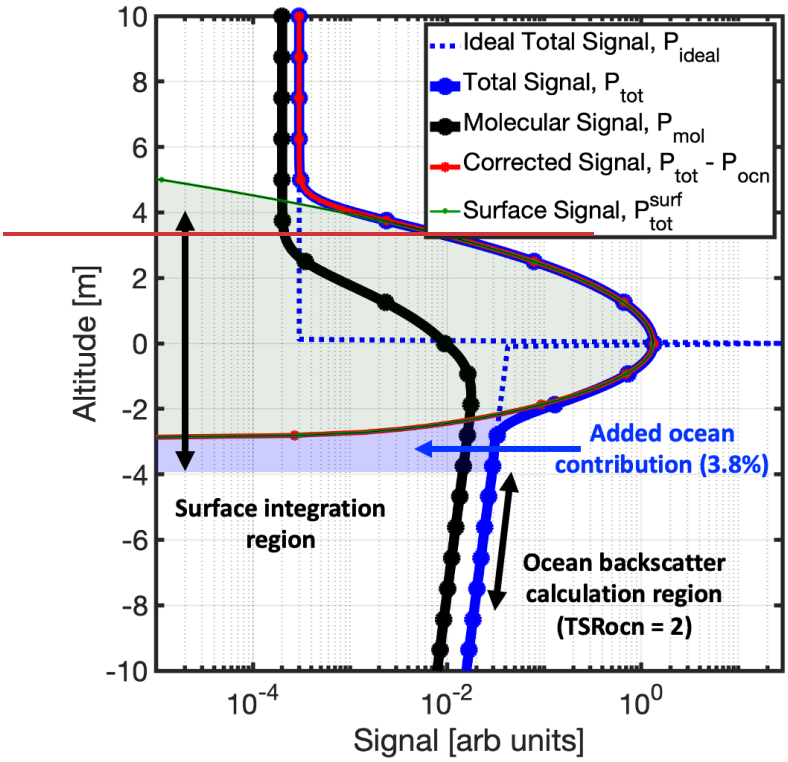

Figure 1: Visualization of HSRL-2 measurement signals as described in Eqs. 6 – 8. Dashed line denotes ideal total backscatter signal from the atmosphere, surface reflection, and the ocean subsurface. Blue and black lines denote measured signals from total and molecular scattering channels, respectively. Red and green lines show the ocean corrected signal and the ocean surface backscatter, respectively. Dots indicate the altitudes of digitized samples. The sampling rate is 120 MHz, resulting in a vertical spacing of 1.25 m in the atmosphere and 0.94 m in the ocean.

It is seen from Fig. 1 and Eq. 8b that the surface component P_{tot}^{surf} of the measured signal P_{tot} is not localized to the surface but is instead spread above and below the surface via convolution with the system response function. The atmosphere and ocean components of P_{tot} are also impacted by the convolution as is P_{mol}. Rearranging Eq. 8 and integrating the total surface backscatter component over the full vertical extent of the system response function (i.e., to ±Δz), the surface response function can be eliminated in the representation of β_{surf} as shown in Eq. 9.

$$\beta_{surf} = \frac{1}{G_{mol} G_{i2}} \frac{r_s^2}{T^2(r_s)} \int_{r_s-\Delta z}^{r_s+\Delta z} P_{tot}^{surf}(r)\, dr \quad (9)$$

Of course, the measurement that can be accessed is P_{tot}, not the surface component P_{tot}^{surf}. If P_{tot} were substituted for P_{tot}^{surf} in Eq. 9, β_{surf} would be overestimated due to the contribution of ocean subsurface backscatter. The atmospheric contribution is negligible (i.e., <0.05%) and can be ignored. The magnitude of the contribution of the ocean subsurface scattering depends on the level of ocean particulate (hydrosol) and as well as molecular seawater backscatter. The magnitude of this scattering relative to the surface backscatter can impact the retrieved surface ~~surface~~ wind speed accuracy. For example, at U = 7 m s^{-1} and assuming pure seawater (i.e., no hydrosols), the integrated total surface signal would be 5.7% higher than the integrated surface backscatter~~. if the ocean subsurface scattering is not accounted for in the calculation.~~ This results in a decrease of 0.75 m s^{-1} (-11% error) in the estimated surface ~~surface~~ wind speed. At a 20 m s^{-1} surface ~~surface~~ wind speed, the error in the calculated surface ~~surface~~ wind speeds results in a decrease by 2.7 m s^{-1} (-14% error). The ocean subsurface correction becomes less as the particulate scattering (or absorption) increases due to increased attenuation in the seawater and therefore contributes less over the integration window around the ocean surface. Therefore, the ocean ~~of the ocean~~ subsurface contribution is higher for clear water compared to turbid water. For example, in~~signal, as for~~ the case illustrated in Fig. 1, ~~for which~~ the seawater particulate and~~ocean~~ molecular scattering are equal, resulting in a contribution of only 3.8% to the integrated surface backscatter as compared to the no ~~and~~ particulate scattering noted above of 5.7%.~~are equal and the integrated subsurface signal is 3.8% higher.~~ The atmospheric signal contribution is much less (~100 times smaller) than the ocean subsurface signal and therefore its contribution is considered negligible. Fortunately, the ~~HSRL technique along with the~~ high vertical resolution of the HSRL-2 instrument enables the ocean subsurface contribution to be estimated. The separation of the molecular signal~~They~~ also enables~~enable~~ estimation of the two-way transmittance, T^2, and ~~molecular~~ gain factor, G_{mol}, in Eq. 9.

For the HSRL-2 instrument, the two-way transmittance is determined directly from the measured molecular channel, P_{mol}. The two-way total (particulate and molecular attenuation) transmittance to the surface can be calculated~~estimated~~ as follows,

$$T^2(r_{ns}) = \frac{1}{G_{mol}} \frac{\overline{P_{mol}(r_{ns}) r_{ns}^2}}{F(r_{ns}) \beta_m^{\parallel}(r_{ns})}, \quad (10)$$

where F is the iodine vapor filter function (known from lab and in-flight calibration), $\beta_m^{\parallel}$ is the molecular backscatter coefficient for the atmosphere (computed from pressure and temperature data from a reanalysis model), and $\overline{P_{mol}(r_{ns}) r_{ns}^2}$ is the range-scaled molecular channel signal near the ocean surface (where r_{ns} is the near-surface range). In practice, this is computed by averaging data from 60 m to 180 m above the surface. This range is somewhat arbitrary but is chosen as a balance between ensuring that the signal does not include any of the surface reflectance and low enough to capture most of the attenuation down to the surface. Substituting Eq. 10 into Eq. 9, one can solve for the surface backscatter,

$$\beta_{surf} = \frac{1}{G_{i2}} \frac{\int_{r_s-\Delta z}^{r_s+\Delta z} r^2 P_{tot}^{surf}(r) dr}{\frac{\overline{P_{mol}(r_{ns}) r_{ns}^2}}{F(r_{ns}) \beta_m^{\parallel}(r_{ns})}}. \quad (11)$$

To account for the ~~atmosphere and~~ ocean subsurface contributions to the measured signal, Eq. 6 can be rearranged as

$$P_{tot}^{surf}(r) = P_{tot} - P_{tot}^{atm}(r) - P_{tot}^{ocn}(r). \quad (12)$$

A benefit of~~Unique to~~ the HSRL-2 ~~retrieval algorithm is that~~retrieval algorithm is that one can use the molecular channel signal to determine the ocean signal near the surface (see Fig. 1). ~~To determine the near-surface ocean signal~~To determine the near-surface ocean signal, an estimate of the total ocean scattering ratio (TSR) is employed, which is the ratio of molecular + hydrosol backscatter divided by molecular backscatter. An estimate of the near-surface TSR, ($\overline{TSR_{ocn}}$) is computed using the quotient of the total and molecular channels (P_{tot} / P_{mol}) averaged over a small range of depths just below the depth at which the surface signal response goes to zero, as follows:

$$\overline{TSR_{ocn}} \equiv \overline{\left(\frac{\beta_p + \beta_m}{\beta_m}\right)} = \frac{F_{ocn}(r)}{G_{i2}\Delta r} \int_{r_s+\Delta z}^{r_s+2\Delta z} \frac{P_{tot}(r)}{P_{mol}(r)} dr \quad (13)$$

where F_{ocn} accounts for the spectral transmission of the molecular seawater backscatter through the iodine vapor filter and is determined via in-flight and laboratory calibrations. The ocean subsurface component of the total channel backscatter is estimated as follows:

$$P_{tot}^{ocn}(r) = \overline{TSR_{ocn}} G_{i2} \frac{P_{mol}(r)}{F_{ocn}(r)}, below\ the\ surface\ (r > r_s) \quad (14)$$

Here the assumption is that the TSR is vertically constant near the surface over the 0.5 s (~75 m horizontal resolution) integration of the lidar signals.~~:~~ Combining Eqs. 11, 12, and 14 and ignoring the atmospheric contribution P_{tot}^{atm} to the total channel signal, one can compute the absolute surface backscatter using the two measured channels as

$$\beta_{surf} = \frac{\int_{r_s-\Delta z}^{r_s+\Delta z} \left(\frac{P_{tot}(r)}{G_{i2}} - \overline{TSR_{ocn}} * P_{mol}(r)\right) r^2 dr}{\frac{\overline{P_{mol}(r_{ns}) r_{ns}^2}}{F_{atm}(r_{ns}) \beta_m^{\parallel}(r_{ns})}}. \quad (15)$$

The use of the molecular channel in this way cancels out absolute system gain constant~~constants~~ (G_{mol} ~~and G_{tot}~~), provides an estimate of the two-way transmittance of the atmosphere, and enables subtraction of ocean subsurface backscatter. It does not require precise knowledge of the system response function or any other assumptions. With Eq. 15, one can calculate the wave-slope variance through Eq. 2 and then use Eqs. 3.1 – 3.3 to derive surface wind speeds.

2.2 ACTIVATE Mission Description

An ideal data set to assess the HSRL-2 ocean surface wind speed product comes from ACTIVATE, which is a NASA Earth Venture Suborbital-3 (EVS-3) mission. The primary aim of ACTIVATE is to improve knowledge of aerosol-cloud-meteorology interactions, which are linked to the highest uncertainty among components contributing to total anthropogenic radiative forcing (Bellouin et al., 2020). There are three major scientific objectives: (i) characterize interrelationships between aerosol particle number concentration (N_a), CCN concentration, and cloud drop number concentration (N_d) with the goal of decreasing uncertainty in model parameterizations of droplet activation; (ii) advance process-level knowledge and simulation of cloud microphysical and macrophysical properties, including the coupling of aerosol effects on clouds and cloud effects on aerosol particles; and (iii) assess remote sensing capabilities to retrieve geophysical variables related to aerosol-cloud interactions. This study focuses on the third objective, which has already received attention with ACTIVATE data for retrievals other than ocean surface wind speeds (Chemyakin et al., 2023; Schlosser et al., 2022; Ferrare et al., 2023; Van Diedenhoven et al., 2022). ACTIVATE built a high volume of flight data statistics over the Western North Atlantic Ocean (WNAO) by flying six deployments across three years (2020 – 2022), with a winter and summer deployment each year (Sorooshian et al., 2023). Winter deployments included the following date ranges: 14 February – 12 March (2020), 27 January – 2 April (2021), 30 November 2021 – 29 March (2022). Summer deployments were as follows: 13 August – 30 September (2020), 13 May – 30 June (2021), 3 May – 18 June (2022). Across all three years, 90 King Air flights during the winter deployment were performed with 373 dropsondes launched while 78 flights during the summer deployment took place with 412 dropsondes launched.

Field Code Changed

Two NASA Langley aircraft flew in spatial and temporal coordination for the majority of the total flights (162 of 179). A "stacked" flight strategy was developed where a low-flying aircraft collected in situ data in and just above the MABL while a high-flying aircraft simultaneously provided remote sensing retrievals well above the MABL. In doing so, the stacked aircraft would simultaneously obtain data relevant to aerosol-cloud-meteorology interactions in the same column of the atmosphere and provide a complete picture of the lower troposphere (Sorooshian et al., 2019). In situ measurements of gases, particles, meteorological variables, and cloud properties were conducted by a HU-25 Falcon flying in and above the MABL (< 5 km). The high-flying aircraft (~9 km) was a King Air whose payload included the NASA Goddard Institute for Space Studies (GISS) Research Scanning Polarimeter (RSP) and the two instruments relevant to this work: the NASA LaRC HSRL-2 and the NCAR AVAPS dropsondes (NCAR, 1993). An advantage of the joint deployment of HSRL-2 and AVAPS dropsondes on the King Air is that the data are spatially synchronized at launch, with wind drift of the dropsondes during descent accounted for with procedures summarized in Sect. 2.3.

Field Code Changed

The rationale to fly over the WNAO in different seasons was to collect data across a wide range of aerosol and meteorological regimes, with the latter promoting a broad range of cloud conditions (Painemal et al., 2021). A significant meteorological

~~feature is the North Atlantic Oscillation, which is the oscillation between the Bermuda-Azores High (high pressure system) and the Icelandic Low (low pressure system) (Lamb and Peppler, 1987). In the summer, the Bermuda-Azores High is at its peak and introduces easterly and southwesterly trade winds (Sorooshian et al., 2020). Starting in the fall, the Icelandic Low becomes prominent and introduces westerly winds in the boundary layer. The balancing act between these pressure systems dictates the climate of the North Atlantic and the prevailing transport processes (Li et al., 2002; Christoudias et al., 2012; Creilson et al., 2003). These transport processes that vary seasonally explain why winter flights coincided with more offshore (westerly) flow containing aerosol types impacted by anthropogenic influence (e.g., Corral et al., 2022), whereas summer flights included more influence from wildfire emissions and African dust among other sources both natural and anthropogenic in nature (Mardi et al., 2021; Aldhaif et al., 2020). Winds and turbulence tend to be stronger in the winter due to higher temperature gradients between the air and the ocean (Brunke et al., 2022), resulting in a higher fraction of available aerosol particles in the MABL that activate into cloud droplets in winter coinciding with cold air outbreaks as compared to summer (Dadashazar et al., 2021; Kirschler et al., 2022; Kirschler et al., 2023; Painemal et al., 2023).~~

Field Code Changed

~~**2.3 Dropsondes**~~

~~The AVAPS system utilized the newer, more reliable NRD41 mini sondes for the ACTIVATE mission. In addition to being smaller, their launching hardware was updated to increase reliability for launches. A variable number of dropsondes were launched per flight, usually 3 to 4 for routine flights, with more being launched for specific targeted flight opportunities.~~

In addition to the specular reflection from the surface, whitecaps or sea foam can increase the lidar backscatter signal. As noted in Josset et al. (2010b), the contribution of scattering by the whitecaps on the ocean surface has been treated as Lambertian scattering. There is a wavelength dependence of the scattering at longer wavelengths due to the water absorption, based on measurements presented by Dierssen (2019) covering wavelengths from 0.4 – 2.5 µm. Measurements presented here are at 532 nm, a region of the visible spectrum where scattering from foam is relatively constant with wavelength. The contribution of whitecaps is typically modeled with a constant average reflectance and an effective area weighted fraction that varies with surface wind speed (Whitlock et al., 1982; Koepke, 1984; Gordon and Wang, 1994; Moore et al., 2000). Following Moore et al. (2000), we have estimated the average reflectance due to the whitecaps as a function of surface wind speed and the difference becomes > 1 m s^{-1} for surface wind speeds > 15 m s^{-1} based on this relationship. As presented below, there are limited data (49 data points) above 13.3 m s^{-1} that can be compared to the dropsonde surface wind speeds to evaluate this relationship. Moreover, since the correction depends on surface wind speed, an iterative calculation is required to use this relationship as the backscatter is dependent on wind speed.

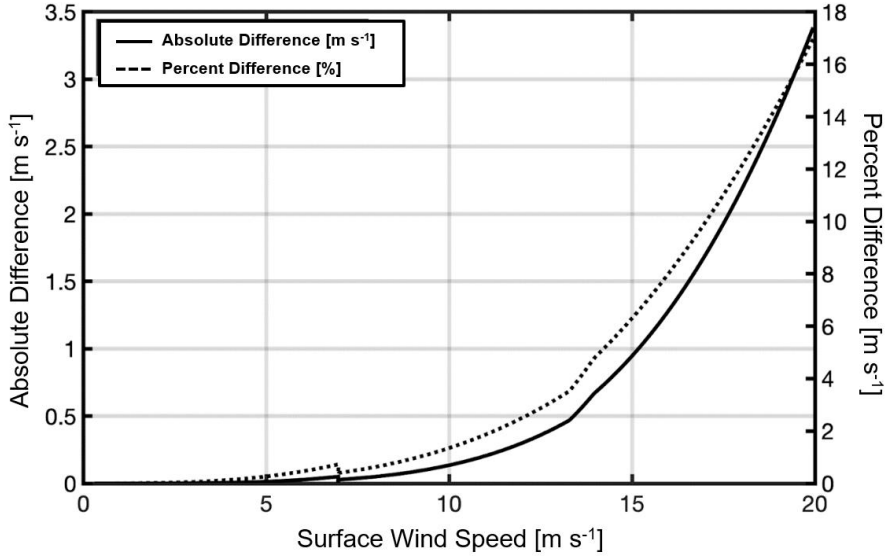

Figure 2. Estimated absolute difference in calculated~~With response times much less than 1 second, AVAPS measures position, wind speed (with 0.5 m s^{-1} uncertainty) (Vömel and Dunion, 2023), and state variables such as pressure, temperature, and humidity, with these data being sampled all the way to ~6 m above the ocean surface. The data are then post processed via NCAR's Atmospheric Sounding Processing Environment (ASPEN) software where any spurious data are removed including any data returned from the ocean surface itself (Martin and Suhr, 2021). More details on the AVAPS system and its usage on other aircraft and missions can be found in Vömel et al. (2021) and Vömel et al. (2023). Not many studies exist on wind speed validation of aircraft instruments with dropsondes (Bedka et al., 2021), so this study also highlights the potential of using dropsondes to validate aircraft wind speed data.~~

~~Because this study focuses on HSRL-2 retrievals of ocean~~**, surface wind speed if reflectance from whitecaps is not included. The lidar surface backscatter is higher than the specular reflectance if whitecaps are present, which results in a lower estimated surface** ~~data, dropsonde~~ **wind speed if not accounted for in the retrieval.**

Alternatively, Hu et al. (2008)~~measurements closest to the 10-m neutral stability height are the primary focus from AVAPS. A map of all 577 dropsondes~~ used a full month of CALIPSO integrated surface depolarization ratio (ratio of the integrated cross polarized channel to the integrated co-polarized channel across the surface) and applied an empirical correction to the reflectance that was determined using AMSR-E data as the ground-truth data set to increase the correlation of the data sets. The correlation was based on much more data than the ACTIVATE matchups between HSRL-2 and dropsondes, limiting the utility

Formatted: Default Paragraph Font, Font: 9 pt, Bold

Formatted: Default Paragraph Font, Font: 9 pt, Bold

of a similar analysis with the HSRL-2. In addition, there are significant differences in the configurations of CALIPSO and HSRL-2 that limit implementation of the same empirical relationship. First, CALIPSO's integrated surface depolarization includes the subsurface contributions due to its 30 m vertical resolution, whereas the HSRL-2 surface depolarization is integrated over only a few meters as ~~in this study from 2020 to 2022 is~~ shown in Fig. 1. Second, the CALIPSO data is based on global data, which is dominated by oligotrophic (clear) waters, whereas a significant fraction of the HSRL-2 - dropsonde comparisons are from eutrophic and mesotrophic waters near the coast and along the shelf. Third, there is a significant difference in footprint size between HSRL-2 and CALIPSO (8 m versus 90 m), with HSRL-2's instantaneous footprint area being greater than 2 orders of magnitude smaller and, considering HSRL-2's along-track averaging (100 laser shots) compared to CALIPSO's single shot data, greater than one order of magnitude smaller in terms of area over which surface depolarization is integrated.~~2.~~

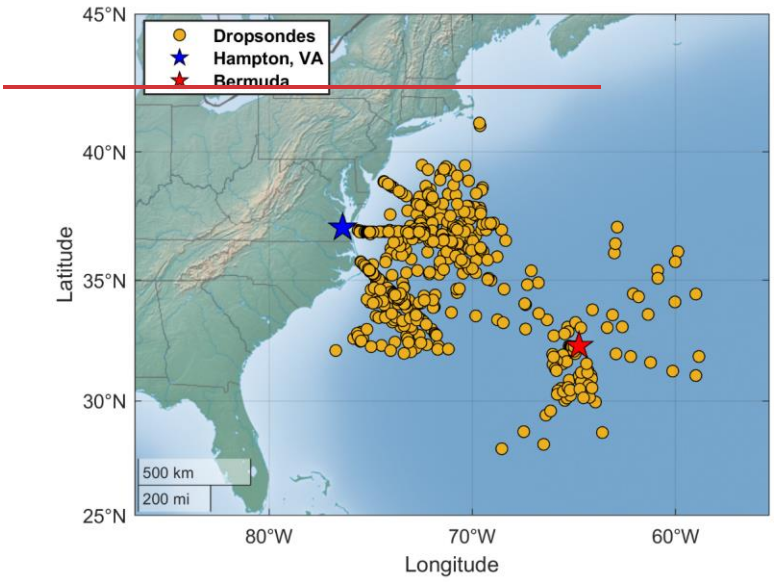

2.5~~**Figure 2: Map of 577 ACTIVATE dropsondes launched from the King Air between 2020 and 2022 that are used in this wind speed intercomparison study.**~~

~~2.4 Data~~ Collocation and Statistical Procedures~~Procedure~~

~~A description of the collocation procedure is provided to describe how the wind speed data intercomparisons between the dropsondes and the HSRL-2 are performed.~~ Since surface ~~surface~~ wind speeds ~~at the surface~~ are the focus of this study, first

Formatted: Normal, Left, Don't keep with next

the dropsonde wind speed data points closest to 10 m (altitude of 11.56 m ± 3.19 m for the 577 points) above sea level are recorded for each launch (multiple launches per flight) to allow meaningful comparison with the HSRL-2 surface wind speeds.). Since one data point was taken per dropsonde for each flight, there are 160 recorded dropsonde measurements for 2020, 245 measurements for 2021, and 335 measurements for 2022. Then, the HSRL-2 surface surface wind speed retrieval closest in space and time to the corresponding dropsonde wind speed measurement is recorded. Note that there are two HSRL-2 data sets collocated with the dropsonde measurements, one calculated from the Hu08 model and the other from the CM54 model, to allow for comparison of these parameterizations in both the case studies and cumulative results detailed in Sects. 2 and 3. Collocation between the HSRL-2 and the dropsondes is constrained to below 30 km horizontally and below 15 minutes temporally to remove outliers while trying to maximizepreserving the maximum number of data points to be used in the study. since data could only be collected in cloud-free or broken cloud conditions, which will be further discussed in Sect. 3.2. Further constraining these distance and time conditions would eliminate more data points with negligible improvement toon the statistics as shown by Figs. S1 and S2 in the supplement. Due to missing data in the HSRL-2 data set and the removal of outliers based on collocation constraints, a total of 577 data points areis available for comparison between the dropsondes and the HSRL-2 (Fig. 3).

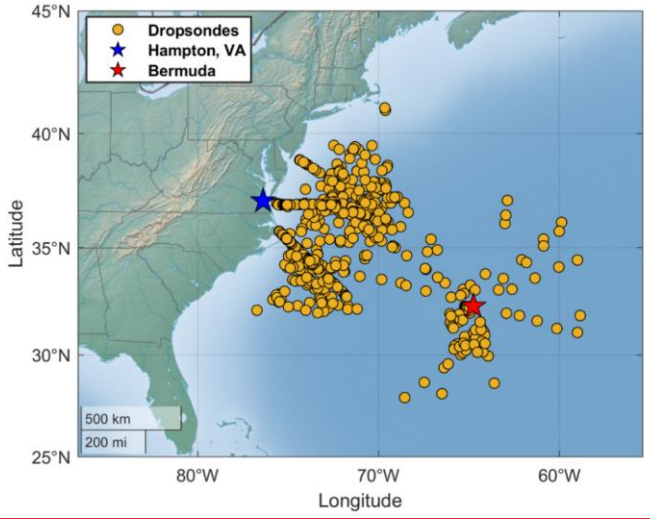

2).

Figure 3: Map of 577 ACTIVATE dropsondes launched from the King Air between 2020 and 2022 that are used to evaluate the HSRL-2 surface wind speed retrievals introduced in this study.

Formatted: Centered

Formatted: Line spacing: single

Formatted: Font: 9 pt, Bold

After~~An example flight, Research Flight 29 on 28 August 2020, showcases~~ the ~~collocation method made possible by ACTIVATE's flight strategy (Fig. 3). This flight is ideal to use for this purpose due to an above average number of dropsondes launched and its planned coordination with CALIPSO.~~

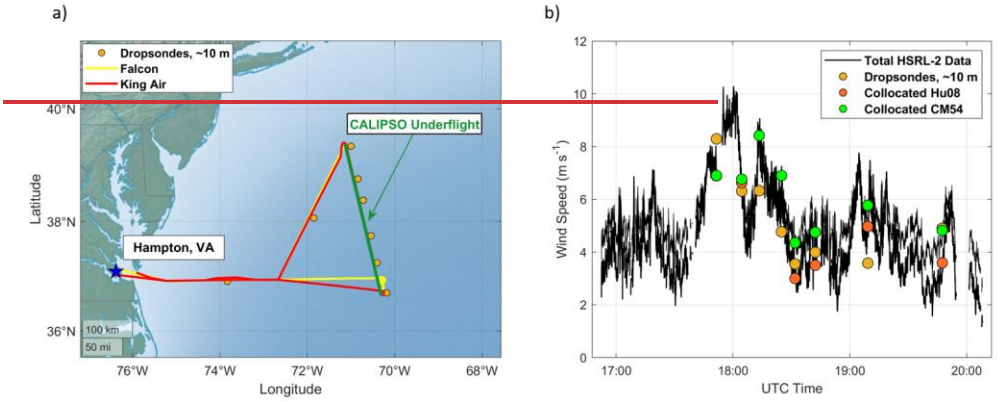

~~**Figure 3: a) Flight map of the King Air and Falcon from Research Flight 29 on 28 August 2020, along with dropsonde locations at the ~10 m neutral stability height, where the green line indicates the flight leg when the aircraft were spatiotemporally coordinated with the CALIPSO satellite. b) Time series of wind speed data from HSRL-2 and dropsondes for the same flight, where lines signify total HSRL-2 wind speed data and circles indicate collocated wind speed data points used in analysis. A few collocated Hu08 and CM54 wind speed data points are on top of each other owing to similar values.**~~

~~The representative flight on 28 August was a cloud-free day and consisted of the King Air and Falcon flying in the standard flight pattern termed a "statistical survey", comprised of repeated stair-stepping legs by the Falcon to probe areas within and just above the MABL (Sorooshian et al., 2023; Dadashazar et al., 2022). During this flight, the aircraft were coordinated with the CALIPSO satellite to allow comparison of ACTIVATE's remote sensing retrievals with satellite retrievals; these types of coordinated underflights of CALIPSO were conducted in cloud-free conditions largely to intercompare aerosol measurements. Eight dropsondes were launched, six of which coincided with the CALIPSO overpass (Fig. 3a). Figure 3b highlights the results of applying this collocation method, showing that the eight collocated HSRL-2 wind speed data points agreed within ~1.2 m s^{-1} of the dropsonde winds on average. However, the error between the HSRL-2 and dropsonde wind speeds reaches ~2 m s^{-1} for two pairs of collocated points, which is higher than the reported error shown later in Sect. 3.1. Further analysis that quantifies the variance of the HSRL-2 wind speed retrieval in the region of the dropsonde measurement is needed since the procedure outlined relies on collocating singular points. Therefore, information on potential geophysical variability and/or variability in the retrieval itself may not be captured. Also, it is observed that Hu08 and CM54 wind speeds significantly differ for wind speeds below 7 m s^{-1} due to the difference in parameterizations as outlined in Eq. 3.1, leading to Hu08 underestimating dropsonde wind speeds and CM54 overestimating dropsonde wind speeds at various times in Fig. 3b. Although the collocation procedure potentially introduces additional variability in the HSRL-2 wind speed retrievals, Research Flight 29 highlights the~~

~~benefits of ACTIVATE's joint deployment of the HSRL-2 and the dropsondes on the King Air for the collection of~~ surface wind speed data are prepared using the procedure above, scatterplots~~.~~

~~2.5 Statistical Analysis Procedure~~

~~Scatterplots~~ along with the correlation coefficient (r), linear regression, and ordinary least squares bisector regression (OLS-bisector) are used to visually demonstrate how well HSRL-2 surface ~~surface~~ wind speed data match dropsonde data and show any potential variability in the data. Since OLS-~~least squares~~ bisector is less~~not a~~ common than linear regression ~~technique~~, a brief explanation of their differences~~how it differs from linear regression~~ is provided. In linear regression, X~~x~~ is treated as the independent variable while Y~~y~~ is treated as the dependent variable. In other words, one observes how Y~~y~~ varies with changes to fixed X~~x~~ values. OLS-~~In the least squares~~ bisector is known as an errors-in-variable regression technique, where X and Y are~~method,~~ both ~~x and y are assumed to be~~ dependent variables and thus both subject to error. OLS-bisector regresses Y on X (standard OLS) and then regresses X on Y (inverse OLS), then bisects the angle of these two ~~(Ricker, 1973). Therefore, the~~ regression lines (Ricker, 1973). Although other errors-in-variable techniques exist (e.g., Deming regression, orthogonal distance regression), OLS-bisector is chosen because it calculates the error ~~is performed assuming error is~~ present in both data sets using the bisector rather than assuming an error a priori like the examples mentioned (Wu and Yu, 2018). After performing these regressions, histograms of surface~~x, which accounts for the variability in the dropsonde wind speeds. Histograms of~~ wind speed deltas, which are defined as HSRL-2 surface ~~surface~~ wind speed minus dropsonde surface ~~surface~~ wind speed, are ~~also~~ created to ~~more easily~~ show the distribution and spread of the data more easily. The mean and ~~. Mean,~~ standard deviation (STD), of the surface~~25th percentile ($Q1$), and 75th percentile ($Q3$) of the~~ wind speed deltas are computed and then used to define the mean error (mean ± ~~to quantify the bias and variability of the HSRL-2 wind speeds relative to the dropsonde wind speeds. The mean and~~ STD). This metric is used to evaluate how accurately the HSRL-2 retrieves surface wind speeds. ~~are calculated as:~~

Formatted: Font: Not Italic

3 Results and Discussion

~~3.1 HSRL-2 – Dropsonde Comparisons~~

~~Observations collected from three years of ACTIVATE data allow for a comprehensive intercomparison of the HSRL-2 retrievals and dropsonde measurements of ocean surface wind speed. This extensive data set can also be utilized in different wind speed models (Hu08 and CM54, specifically) to observe the effects they have on these intercomparisons. All intercomparison results for both models are shown in Figs. 4 – 8 and Tables 1 – 2.~~

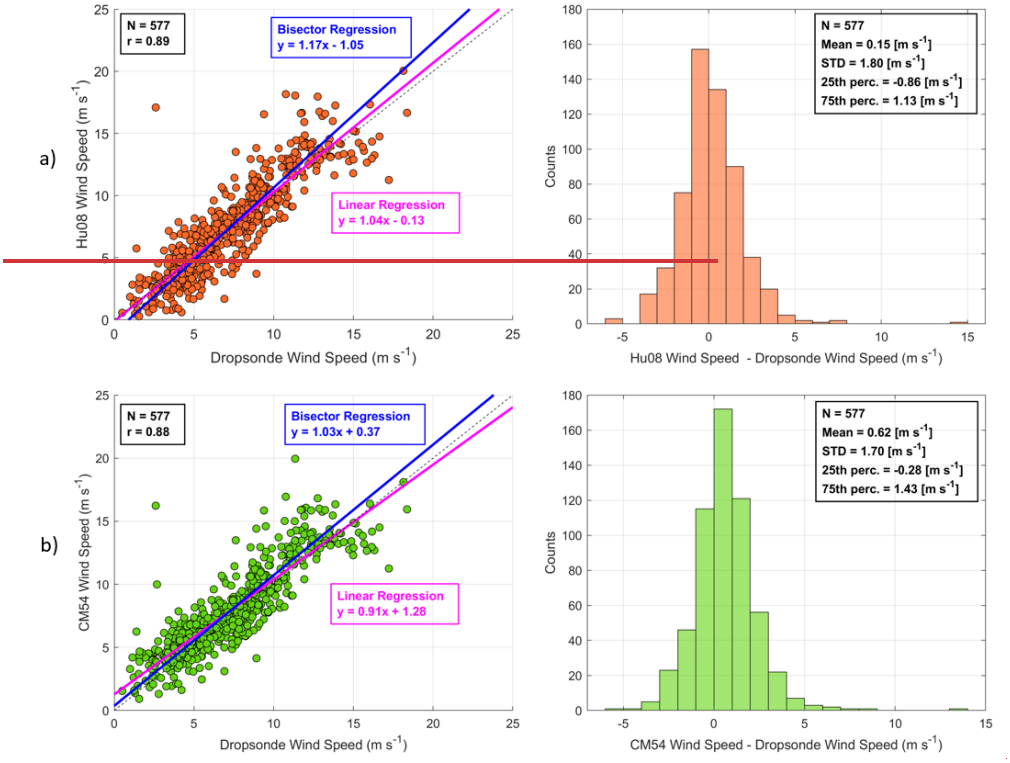

~~**Figure 4: Scatterplots with associated histograms for all HSRL-2 – dropsonde collocated wind speed data points for a) Hu08 and b) CM54 models.**~~ ~~**N represents the number of data points.**~~ **3.1 Case Studies**

Before delving into the HSRL-2 – dropsonde surface wind speed intercomparisons in full statistical detail, surface wind speed data from two ACTIVATE research flights are analyzed: Research Flight 29 on 28 August 2020 and Research Flight 14 on 1 March 2020. These flights are analyzed to demonstrate the ability of the HSRL-2 to 1) provide profiles that show the spatial variability of surface wind speed over time, which are beneficial to observe phenomena like sea-surface temperature dynamics and cloud evolution and 2) sample the surface in broken cloud scenes, showing that the retrievals are not limited to cloud- and aerosol-free conditions like in Hu et al. (2008).

3.1.1 Research Flight 29 on 28 August 2020

Research Flight 29 was a near cloud-free day where an above average number of dropsondes were launched and ACTIVATE's aircraft were coordinated with the CALIPSO satellite overpass. These conditions allow for the examination of how the high horizontal spatial resolution of the HSRL-2 (~75 m along track as mentioned in Sect. 2.4) influences its retrievals and how the data can be used to track sea surface temperature (SST) gradients common to the WNAO (Painemal et al., 2021) as seen in Fig. 4. Note that Fig. 4a uses SST data from Modern-Era Retrospective Analysis for Research and Applications, Version 2 (MERRA-2) (Gelaro et al., 2017) to contextualize the SST gradients present in the WNAO, and no comparisons with MERRA-2 surface wind speed data are performed in this study.

Formatted: Font color: Black

Formatted: Font color: Black

Formatted: Font color: Black

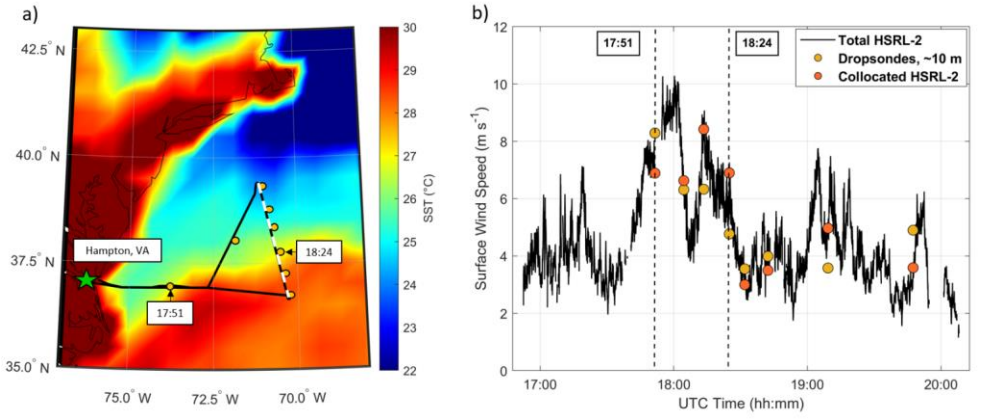

Figure 4: a) Flight map of King Air (black line) and dropsondes (dark yellow circles) overlaid onto map of MERRA-2 mean sea-surface temperature (SST) data (Gmao, 2015) for Research Flight 29 on 28 August 2020. White dashed line corresponds to the CALIPSO overpass coincident with King Air flight path. Time stamps represent where the King Air crosses over sharp SST changes associated with the Gulf Stream. b) Time series of surface wind speed data from HSRL-2 and dropsondes for the same flight, where the black solid line signifies total HSRL-2 surface wind speed data and circles indicate collocated surface wind speed data points. Black dashed lines represent time stamps of interest as indicated in a).

It is seen that changes in the HSRL-2 surface wind speeds (Fig. 4b) correspond with changes in SST (Fig. 4a), especially seen at 17:51 and 18:24 (UTC throughout paper). As the aircraft approaches and crosses the SST boundary at 17:51 (i.e., SST increasing), there is a corresponding increase in surface wind speeds. The reverse observation can be seen when the aircraft approaches and crosses the boundary at 18:24 (i.e., SST decreasing), where surface wind speeds noticeably decrease. Although further analysis is needed to rigorously examine the relationship between surface wind speed and SST, these observations show that the HSRL-2 has the high horizontal spatial resolution needed to probe the fine-scale variability of surface wind speeds and has the potential to improve atmospheric modeling of MABL processes. These profiles capture the spatial gradients

in surface wind speeds that would otherwise not be available with the dropsondes alone, since these instruments can only take point measurements as they drop vertically to the surface and therefore cannot provide the horizontal spatial extent like the derived HSRL-2 surface wind speed product can.

3.1.2 Research Flight 14 on 1 March 2020

Next, Research Flight 14 is shown in Fig. 5 to demonstrate the ability of the HSRL-2 to sample in broken cloud scenes. This flight along with the associated morning flight on 1 March 2020 have been the subject of several studies owing to its coincidence with cold air outbreak conditions (see cloud streets in Fig. 5a) and a flight strategy that allowed for detailed characterization of the evolving aerosol-cloud system as a function of distance offshore (Seethala et al., 2021; Chen et al., 2022; Li et al., 2022; Tornow et al., 2022; Sorooshian et al., 2023). The morning flight focused on a location with very detailed characterization including stacked level flight legs (i.e., termed a "wall") with the Falcon flying below, in, and above clouds, with the King Air flying aloft to further characterize the same region. The afternoon flight consisted of both aircraft flying back to that same location, adjusting the sampling strategy to fly along the boundary layer wind direction in a quasi-Lagrangian fashion to keep studying the evolution of the air mass characterized in the morning. The afternoon flight is chosen because it shows the full range of cloud conditions from clear to completely overcast. Therefore, the HSRL-2 surface wind speed retrievals are able to be evaluated in this range of conditions.

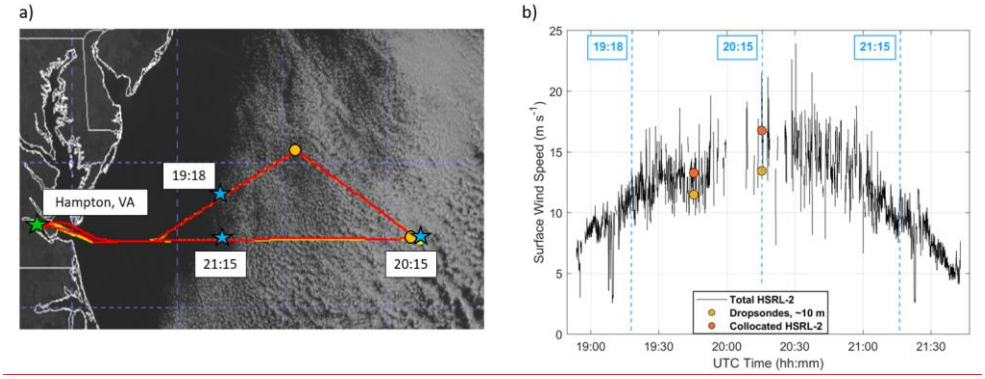

Figure 5: a) Flight map of the King Air (red line), Falcon (yellow line), and dropsondes (dark yellow circles) overlaid onto Geostationary Operational Environmental Satellite (GOES-16) cloud imagery for Research Flight 14 on 1 March 2020. Blue stars represent time stamps where the King Air crosses over from cloud-free to cloudy areas. b) Time series of surface wind speed data from HSRL-2 and dropsondes for the same flight, where lines signify total HSRL-2 surface wind speed data and circles indicate collocated surface wind speed data points. Blue dashed lines represent time stamps of interest as indicated in a).

As the aircraft approaches the cloud scene at 19:18, there is a noticeable and steady increase of HSRL-2 surface wind speeds. The reverse observation is seen when the aircraft approaches 21:15, where the HSRL-2 surface wind speeds start to decrease steadily. As highlighted in the 28 August 2020 case study, the high horizontal spatial resolution of the HSRL-2 retrievals

enables these spatial gradients to be observed. Another important takeaway is the HSRL-2 is still able to sample the surface in cloud scenes, as seen by the almost complete surface wind speed profile in Fig. 5b. Although a gap in data occurs at 20:15 where cloud cover is most substantial, some retrievals are still present in that area. The reason is that the HSRL-2 can probe the surface through gaps between clouds, allowing for the surface wind speed retrievals to take place. Although the HSRL-2 retrievals would be unavailable in overcast cloud scenes, the ability of the instrument to sample the surface in broken cloud fields and not just aerosol- and cloud-free scenes is a significant benefit of the lidar and the HSRL technique.

3.2 HSRL-2 – Dropsonde Comparisons

Now, the collocated HSRL-2 retrievals and dropsonde measurements of surface wind speed are compared and the results are shown in Fig. 6.

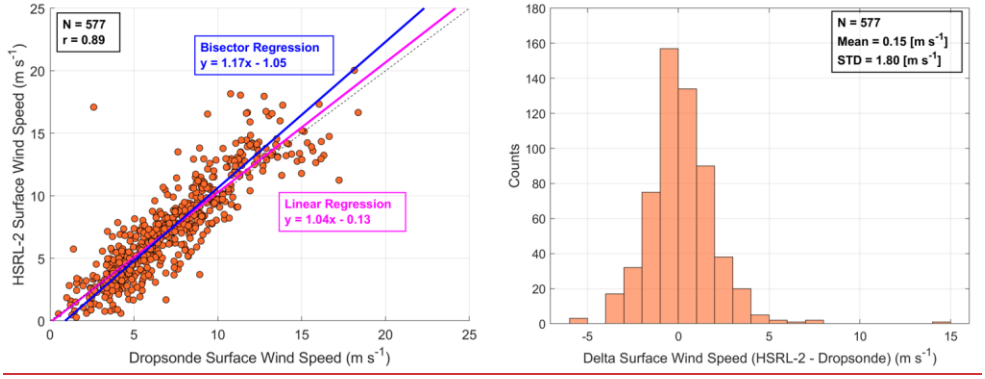

Figure 6: Scatterplots with associated histograms for HSRL-2 – dropsonde collocated surface wind speed data points using ACTIVATE's 2020 – 2022 data set. N represents the number of data points. ~~**- N represents the number of data points.**~~

The comparison yields correlation coefficients of 0.89, slopes of 1.04 and 1.17, and y-intercepts of -0.13 m s^{-1} and -1.05 m s^{-1} for linear and bisector regressions, respectively. Note that the correlation coefficients are the same for linear and bisector regressions throughout this analysis, so they are listed as one value throughout Sect. 3.2. Using the mean and STD values in the same figure, the mean error or accuracy of the HSRL-2 surface wind speed retrievals is 0.15 m s^{-1} ± 1.80 m s^{-1}. These results show that on average, the HSRL-2 slightly overestimates surface wind speeds and the estimation can be off by about 2 m s^{-1} in either direction.

Now that the HSRL-2 retrievals have been broadly evaluated, Fig. 7 shows how their accuracy varies per 1 m s^{-1} interval in surface wind speed. This plot also provides the opportunity to compare the Hu et al. (2008) model with the models proposed by Cox and Munk (1954) and Wu (1990) to see if some of the error in the HSRL-2 retrievals can be attributed to model characteristics.

Formatted: Justified

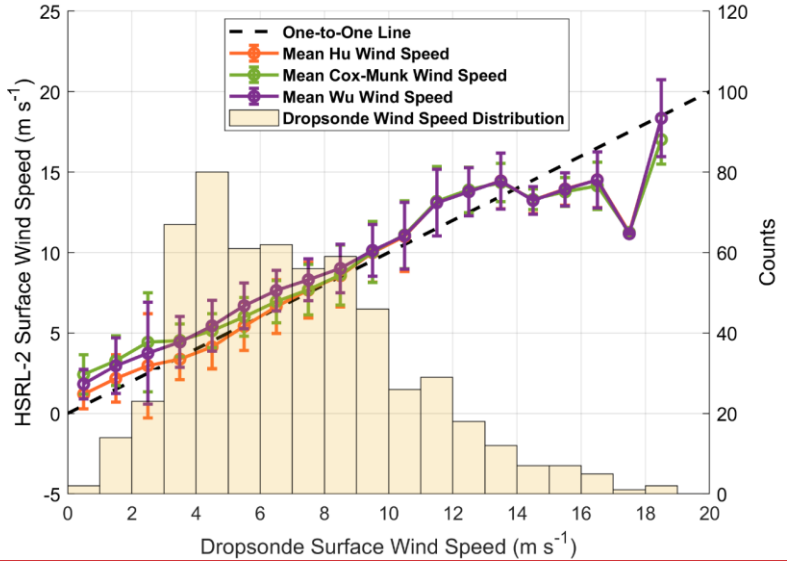

Figure 7: HSRL-2 surface wind speed using Hu, Cox-Munk, and Wu models versus mean dropsonde surface wind speed calculated per 1 m s^{-1} bin. A histogram of dropsonde surface wind speeds is also included to show their distribution.

It is seen that the mean Cox-Munk and Wu surface wind speed values are higher than the mean Hu values from 0 m s^{-1} to 7 m s^{-1}, showing that the Cox-Munk and Wu relationships overestimate dropsonde surface wind speeds more than the Hu relationship. The variability (i.e., STD) around the mean per bin is similar between the three models, which is 1.59 m s^{-1} for Hu, 1.43 m s^{-1} for Cox-Munk, and 1.55 m s^{-1} for Wu on average. Although similar, the STD of the Hu surface wind speeds found here is ~0.4 m s^{-1} lower than the one found in Fig. 6. This could be attributed to an STD not being able to be calculated for the 17 to 18 m s^{-1} bin since it only contained one point.

Although it is apparent Cox-Munk and Wu retrievals overestimate dropsonde observations for surface wind speeds below 7 m s^{-1}, it is still unclear which of the models perform better overall. Therefore, the y-axis from Fig. 7 is converted to wave-slope space and the result of this modification is shown in Fig. 8. HSRL-2 wave-slope is used because it directly reports the original measurements of surface reflectance rather than estimated values of surface wind speed. Using the original data ensures that uncertainty is coming from the actual HSRL-2 – dropsonde comparisons rather than from potential errors in the conversion from wave-slope to surface wind speed.

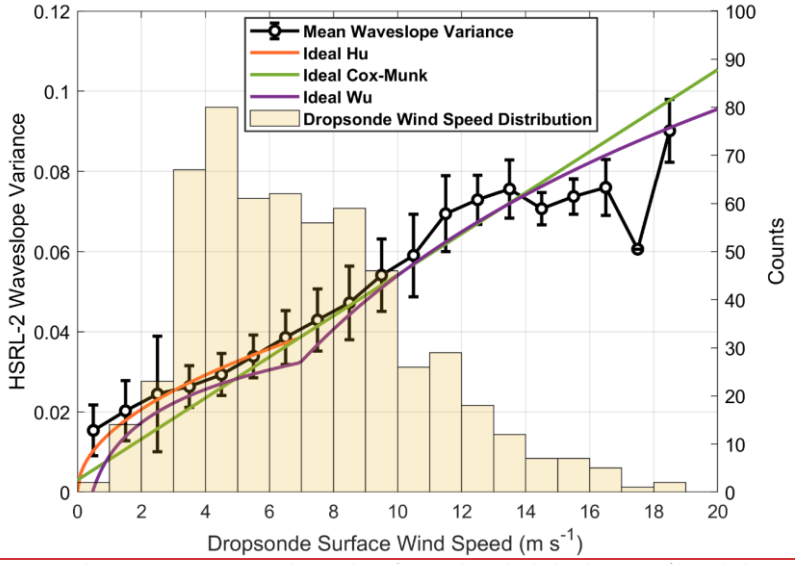

Figure 8: HSRL-2 wave-slope variance versus mean dropsonde surface wind speed calculated per 1 m s^{-1} bin. Ideal Hu, Cox-Munk, and Wu distributions are included to show how well observed dropsonde data match with each parameterization. A histogram of dropsonde surface wind speeds is also included to show their distribution.

From Fig. 8, it is more easily seen how the dropsonde surface wind speed distribution compares with Hu, Cox-Munk, and Wu parameterizations. Dropsonde surface wind speeds match quite closely to Hu and Cox-Munk parameterizations as opposed to the Wu parameterization between 7 m s^{-1} and 13.3 m s^{-1}, although some divergence is seen above ~10.5 m s^{-1}. However, a critical observation that is more apparent in Fig. 8 than Fig. 7 is how the dropsonde data most resemble the Hu distribution for surface wind speeds below 7 m s^{-1}. This improvement is substantial, especially since most of the surface wind speeds in ACTIVATE fall into this category. Surface wind speeds above 13.3 m s^{-1} substantially diverge from all models, especially above 16 m s^{-1}. As mentioned previously, there are few surface wind speed observations in this category, so more measurements are necessary to make meaningful comparisons between the two data sets. Overall, Figs. 7 and 8 demonstrate the benefits of using the Hu parameterization in this study and why surface wind speeds above 13.3 m s^{-1} are not the main focus of the comparisons in this section. Further analysis is warranted to rigorously compare the performance of various surface reflectance models and potentially apply corrections (i.e., whitecap correction for surface wind speeds above 13.3 m s^{-1}), but

the aim of this paper is to evaluate LARC's HSRL-2 surface wind speed retrieval algorithm using the available ground-truth dropsonde measurements.

Now that the Hu relationship has been deemed the more effective model through the preliminary analysis shown in Figs. 7 and 8, a more rigorous statistical analysis is performed for surface wind speeds 1) below 7 m s^{-1} and 2) between 7 m s^{-1} and 13.3 m s^{-1} to assess the overall accuracy of the HSRL-2 retrievals in these categories (Fig. 9).

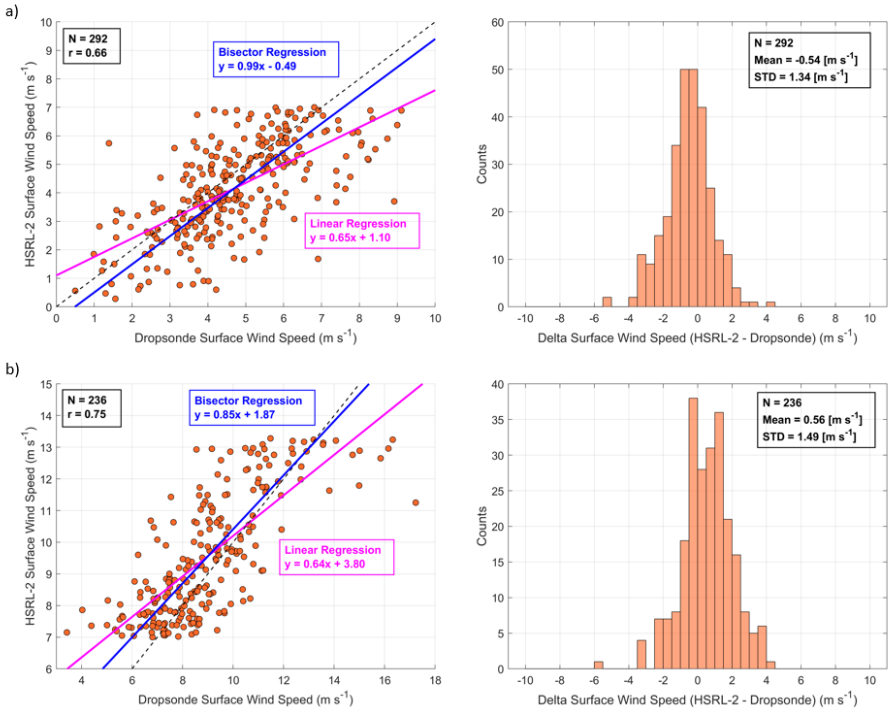
a)
N = 292
r = 0.66
Bisector Regression
y = 0.99x - 0.49
Linear Regression
y = 0.65x + 1.10
HSRL-2 Surface Wind Speed (m s-1)
Dropsonde Surface Wind Speed (m s-1)
N = 292
Mean = -0.54 [m s-1]
STD = 1.34 [m s-1]
Counts
Delta Surface Wind Speed (HSRL-2 - Dropsonde) (m s-1)
b)
N = 236
r = 0.75
Bisector Regression
y = 0.85x + 1.87
Linear Regression
y = 0.64x + 3.80
HSRL-2 Surface Wind Speed (m s-1)
Dropsonde Surface Wind Speed (m s-1)
N = 236
Mean = 0.56 [m s-1]
STD = 1.49 [m s-1]
Counts
Delta Surface Wind Speed (HSRL-2 - Dropsonde) (m s-1)

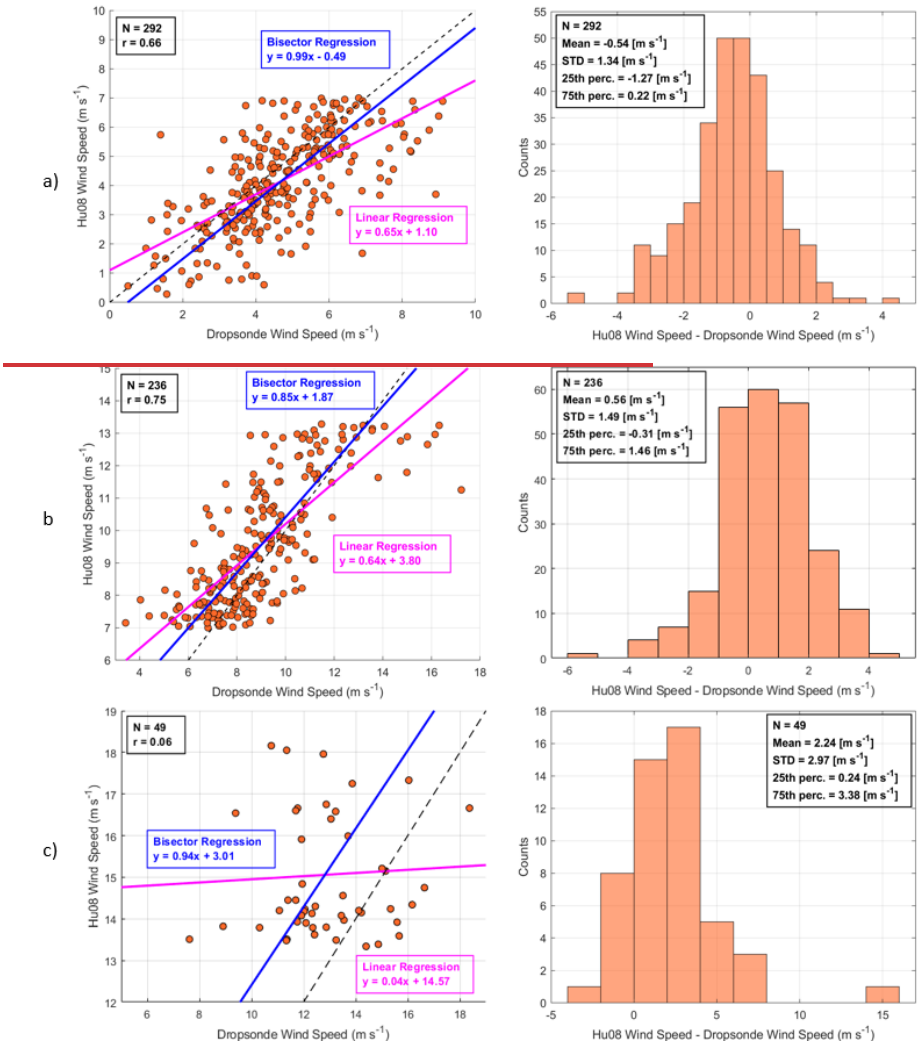

635 **Figure 9:~~5:~~ Scatterplots with associated histograms for HSRL-2~~Hu08~~ – dropsonde collocated surface ~~surface~~ wind speed data points for a) surface wind speeds~~Wind Speed~~ < 7 m s^{-1} and, b) surface wind speeds between 7 m s^{-1} and≤ ~~Wind Speed <~~ 13.3 m s^{-1},~~, and c) Wind Speed ≥ 13.3 m s^{-1}.~~ Note that x- and y-axis ranges vary to better showcase results in individual panels. N represents the number of data points.**

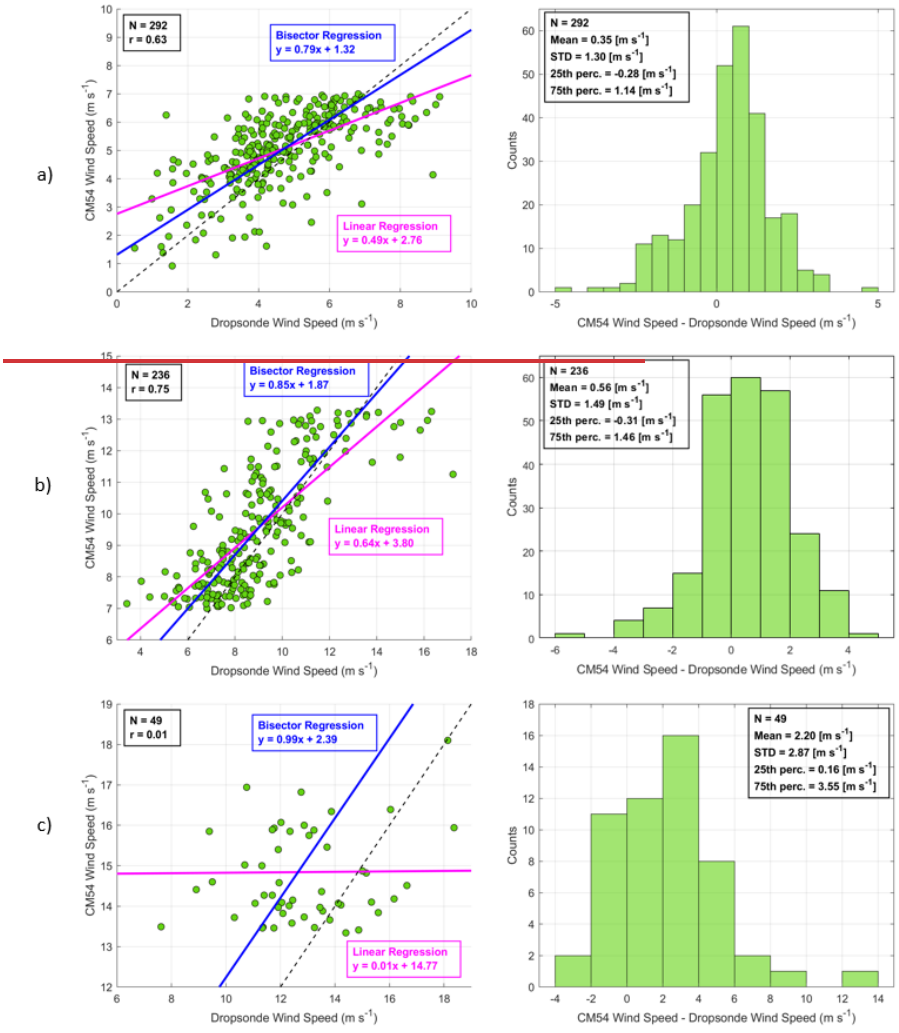

Formatted: Caption, Left, Don't keep with next

640 **Intercomparisons for surface wind speeds below 7 m s^{-1} (Fig. 9a) show correlation coefficients of 0.66, slopes of 0.65 and 0.99, and y-intercepts of 1.10 m s^{-1} and -0.49 m s^{-1} for linear and bisector regressions, respectively. The accuracy of the HSRL-2 retrievals is calculated to be -0.54 m s^{-1} ± 1.34 m s^{-1}, showing that the HSRL-2 on average underestimates surface wind speeds and this**

estimation could vary by ± 1.34 m s^{-1}. For surface wind speeds between 7 m s^{-1} and 13.3 m s^{-1} (Fig. 9b), correlation coefficients of 0.75, slopes of 0.64 and 0.85, and y-intercepts of 3.80 m s^{-1} and 1.87 m s^{-1} are reported for linear and bisector regressions, respectively. The mean error of 0.56 m s^{-1} ± 1.49 m s^{-1} shows that the HSRL-2 overpredicts surface wind speeds by about ~0.5 m s^{-1} on average with a variability of ± ~1.5 m s^{-1}. Therefore, the means from both categories average out to ~0 m s^{-1} since they are approximately the same but in opposite directions. Separating the data into these categories highlight an important result that could not be seen in the cumulative data (Fig. 6): one can expect bias of up to ~0.5 m s^{-1} in either direction and error of up to ~1.5 m s^{-1} on average for most HSRL-2 surface wind speed retrievals in ACTIVATE.~~Figure 6: Scatterplots with associated histograms for CM54 – dropsonde collocated wind speed data points for a) Wind Speed < 7 m s^{-1}, b) 7 m s^{-1} ≤ Wind Speed < 13.3 m s^{-1}, and c) Wind Speed ≥ 13.3 m s^{-1}. Note that x- and y-axis ranges vary to better showcase results in individual panels.~~

Formatted: Justified, Don't keep with next

The data are then divided into winter and summer deployments (dates provided in Sect. 2.1) as shown in Fig. 10 to assess the HSRL-2's retrieval accuracy in different seasons.

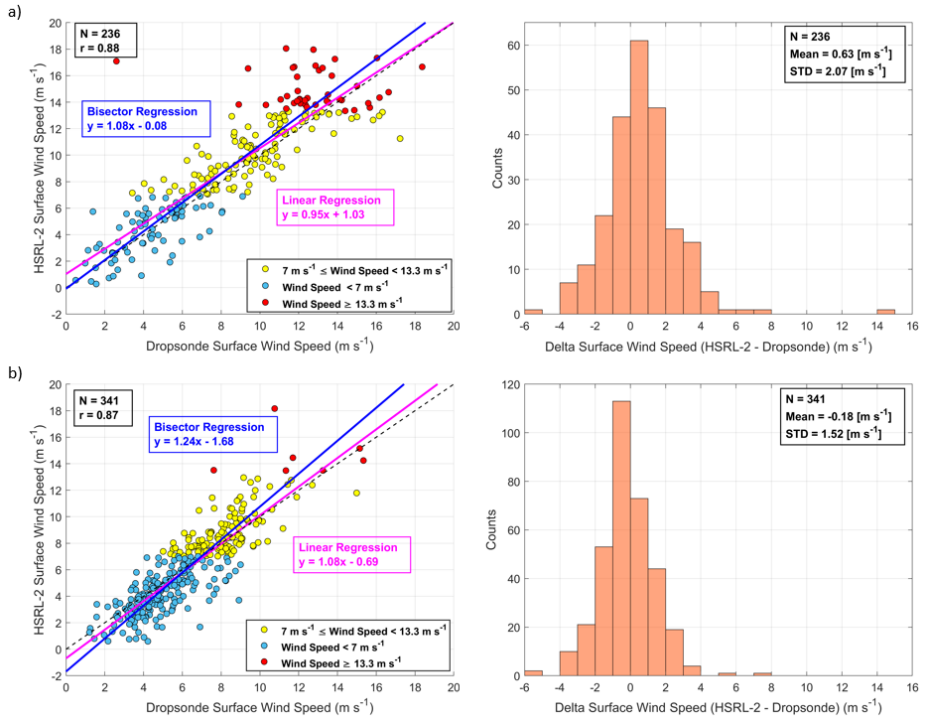

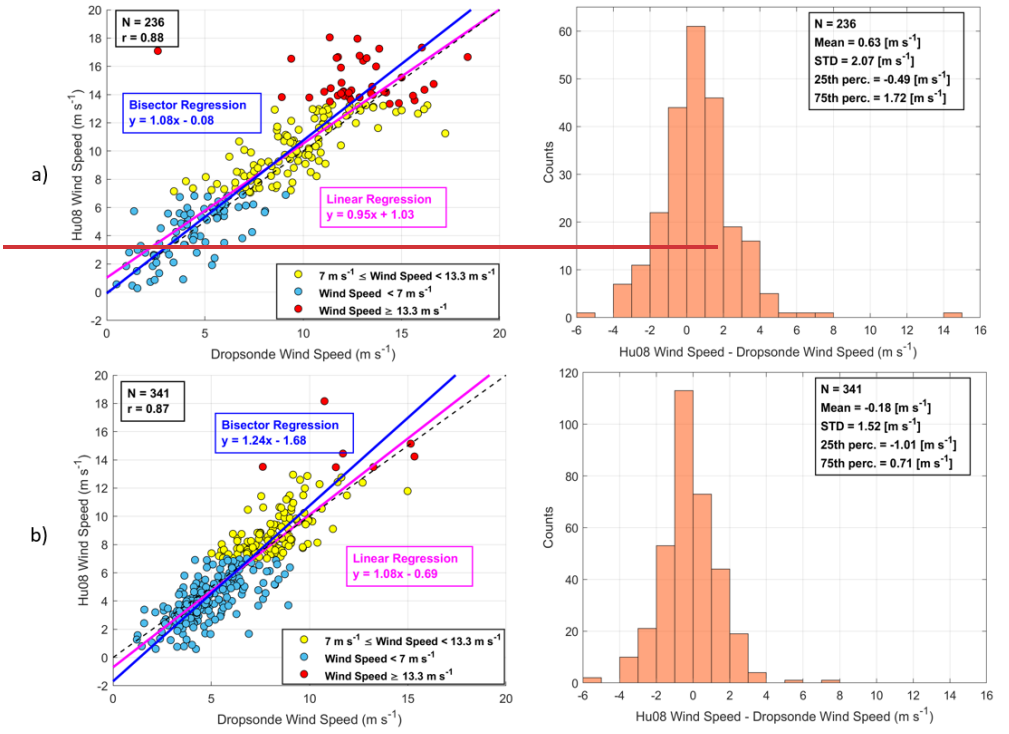

Figure 10:~~7:~~ Scatterplots with associated histograms for HSRL-2~~Hu08~~ – dropsonde collocated surface ~~surface~~ wind speed data points for a) winter and b) summer deployments. Data are highlighted based on surface wind speed categories: 7 m s^{-1} ≤ Wind Speed < 13.3 m s^{-1}, Wind Speed < 7 m s^{-1}, and Wind Speed ≥ 13.3 m s^{-1}. N represents the number of data points.

As seen in Fig. 10a, the winter surface wind speed intercomparisons show correlation coefficients of 0.88, slopes of 0.95 and 1.08, and y-intercepts of 1.03 m s^{-1} and -0.08 m s^{-1} for linear and bisector regressions, respectively. The summer surface wind speed intercomparisons (Fig. 10b) have correlations of 0.87, slopes of 1.08 and 1.24, and y-intercepts of -0.69 m s^{-1} and -1.68 m s^{-1}. Finally, the mean errors for winter and summer, respectively, are reported as 0.63 m s^{-1} ± 2.07 m s^{-1} and -0.18 ± 1.52 m s^{-1}. It is seen that the error in the HSRL-2 estimations of surface wind speeds is larger for winter than summer, most likely due to the higher fraction of surface wind speeds above 13.3 m s^{-1} and lower fraction of them below 7 m s^{-1} in the winter. This observation makes sense because of the increased presence of clouds, precipitation, and whitecaps for the higher surface wind speeds observed in the winter. These observations show that HSRL-2 retrievals of surface wind speed are more accurate in the summer over the winter. However, the HSRL-2 can still make numerous accurate retrievals as shown by the Fig. 10 and the 1

Formatted: Font: 9 pt

Formatted: Don't keep with next

March 2020 research flight discussions. Caution must still be exercised when using data from days featuring turbulent meteorological conditions that could induce whitecaps and/or substantial cloud cover that could limit or even prevent the HSRL-2 from sampling the surface.

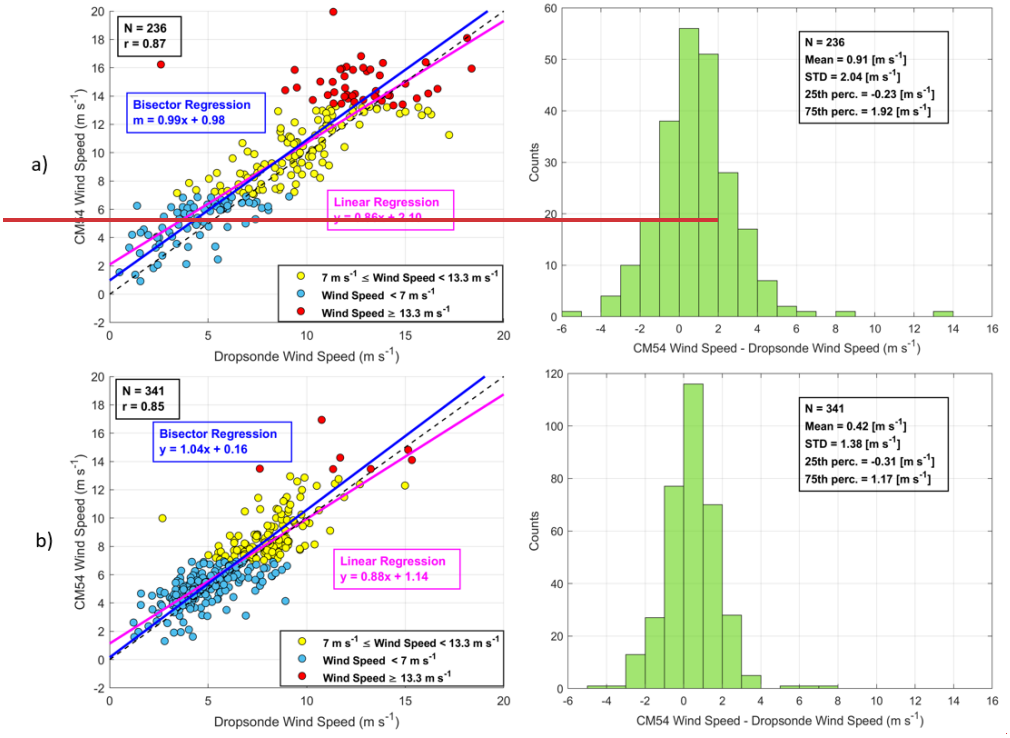

~~Figure 8: Scatterplots with associated histograms for CM54 – dropsonde collocated wind speed data points for a) winter and b) summer deployments.~~

Statistics evaluating the HSRL-2 surface wind speed retrievals (Figs. 6, 9, 10) are summarized in Table 1 for convenience.

Table 1:a: Summary of all HSRL-2Hu08 – dropsonde surface surface wind speed comparison statistics shown in Figs. 4, 5, 7 6, 9, and 10scatterplots. The two values for slope and y-intercept refer to those for the linear and bisector regressions, in that order. R values are the same for both linear and bisector regressions, so they are listed as one value.

	N	r	Slope	Y-intercept [m s^{-1}]	Mean Error [m s^{-1}]
Overall	577	0.89	1.04/1.17	-0.13/-1.05	0.15 ± 1.80
Wind Speed < 7 m s^{-1}	292	0.66	0.65/0.99	1.10/-0.49	-0.54 ± 1.34
7 m s^{-1} ≤ Wind Speed < 13.3 m s^{-1}	236	0.75	0.64/0.85	3.80/1.87	0.56 ± 1.49
Winter	236	0.88	0.95/1.08	1.03/-0.08	0.63 ± 2.07
Summer	341	0.87	1.08/1.24	-0.69/-1.68	-0.18 ± 1.52
N			Slope	Y-intercept [m s^{-1}]	r
Overall	577		1.04/1.17	-0.13/-1.05	0.89
Wind Speed < 7 m s^{-1}	292		0.65/0.99	1.10/-0.49	0.66
7 m s^{-1} ≤ Wind Speed < 13.3 m s^{-1}	236		0.64/0.85	3.80/1.87	0.75
Wind Speed ≥ 13.3 m s^{-1}	49	0.04/0.94	14.57/3.01	0.06	
Winter	236		0.95/1.08	1.03/-0.08	0.88
Summer	341		1.08/1.24	-0.69/-1.68	0.87

Table 1b: Summary of all Hu08 – dropsonde wind speed statistics shown in Figs. 4, 5, 7 histograms.

	N	Mean [m s^{-1}]	STD [m s^{-1}]	25th perc. [m s^{-1}]	75th perc. [m s^{-1}]	Mean Error [m s^{-1}]
Overall	577	0.15	1.80	-0.86	1.13	0.15 ± 1.80
Wind Speed < 7 m s^{-1}	292	-0.54	1.34	-1.27	0.22	-0.54 ± 1.34
7 m s^{-1} ≤ Wind Speed < 13.3 m s^{-1}	236	0.56	1.49	-0.31	1.46	0.56 ± 1.49
Wind Speed ≥ 13.3 m s^{-1}	49	2.24	2.97	0.24	3.38	2.24 ± 2.97
Winter	236	0.63	2.07	-0.49	1.72	0.63 ± 2.07
Summer	341	-0.18	1.52	-1.01	0.71	-0.18 ± 1.52

Table 2a: Summary of all CM54 – dropsonde wind speed statistics shown in Figs. 4, 6, 8 scatterplots. The two values for slope and y-intercept refer to those for the linear and bisector regressions in that order.

Formatted: Font: Not Bold

Formatted: Font: 9 pt, Not Bold

Formatted Table

Formatted: Font: 9 pt

Formatted Table

	N	Slope	Y-intercept [m s^{-1}]	r
Overall	577	0.91/1.03	1.28/0.37	0.88
Wind Speed < 7 m s^{-1}	292	0.49/0.79	2.76/1.32	0.63
7 m s^{-1} ≤ Wind Speed < 13.3 m s^{-1}	236	0.64/0.85	3.80/1.87	0.75
Wind Speed ≥ 13.3 m s^{-1}	49	0.01/0.99	14.77/2.39	0.01
Winter	236	0.86/0.99	2.10/0.98	0.87
Summer	341	0.88/1.04	1.14/0.16	0.85

Table 2b: Summary of all CM54 – dropsonde wind speed statistics shown in Figs. 4, 6, 8 histograms.

	N	Mean [m s^{-1}]	STD [m s^{-1}]	25th perc. [m s^{-1}]	75th perc. [m s^{-1}]	Mean Error [m s^{-1}]
Overall	577	0.62	1.70	-0.28	1.43	0.62 ± 1.70
Wind Speed < 7 m s^{-1}	292	0.35	1.30	-0.28	1.14	0.35 ± 1.30
7 m s^{-1} ≤ Wind Speed < 13.3 m s^{-1}	236	0.56	1.49	-0.31	1.46	0.56 ± 1.49
Wind Speed ≥ 13.3 m s^{-1}	49	2.20	2.87	0.16	3.55	2.20 ± 2.87
Winter	236	0.91	2.04	-0.23	1.92	0.91 ± 2.04
Summer	341	0.42	1.38	-0.31	1.17	0.42 ± 1.38

Strong correlations are seen between dropsonde winds and both Hu08 and CM54 as seen in Fig. 4, with the correlation coefficients being 0.89/0.88 (Hu08/CM54). Biases are 0.15/0.62 m s^{-1} while the STDs are 1.81 m s^{-1}/1.80 m s^{-1}. Regression y-intercepts (linear/bisector) are also similar between the two models (-0.13/-1.05 m s^{-1} for Hu08 and 1.28/0.37 m s^{-1} for CM54), although Hu08 has slightly better performance in the linear fit while CM54 seems to perform better in the bisector fit. As seen by mean and STD values shown in Fig. 4, the error of Hu08 wind speeds is 0.15 m s^{-1} ± 1.80 m s^{-1} while the error of CM54 wind speeds is 0.62 m s^{-1} ± 1.70 m s^{-1}. These results show that both Hu08 and CM54 wind speeds are biased slightly high compared to the dropsonde wind speeds, which is probably due to the influence of high wind speed outliers seen in both the scatterplots and histograms.

To further investigate the source of these bias and variability trends, the data are divided into low (Wind Speed < 7 m s^{-1}), intermediate (7 m s^{-1} ≤ Wind Speed < 13.3 m s^{-1}), and high (Wind Speed ≥ 13.3 m s^{-1}) wind speed regimes as shown in Figs. 5 and 6. These regimes correspond with those that Hu08 delineates in Eqs. 3.1 – 3.3. In the low wind regime, Hu08 is biased low at -0.54 m s^{-1} while CM54 winds are biased high at 0.35 m s^{-1}. Also, the low wind speed regime intercomparisons have the lowest variability compared to those of the intermediate and high wind speed regimes in terms of STD and y-intercept. Based on these observations, the low bias and variability of Hu08 winds below 7 m s^{-1} drive down the bias and variability in

the overall data comparisons. At the same time, both Hu08 and CM54 wind speeds in the high wind speed regime have relatively poor agreement with dropsonde values and increase the bias and variability observed in the intercomparisons. However, most of the data are contained within the low wind speed regime, which mostly offset errors observed in the high wind speed regime.

The wind speed data are also divided into winter and summer deployments (dates provided in Sect. 2.2) as shown in Figs. 7 and 8 to determine if the wind speed intercomparisons have dependence on seasonal factors. Overall, summer intercomparisons perform better than winter ones based on summer's lower bias (0.18/0.42 m s^{-1}) and STD (1.52/1.38 m s^{-1}) values compared to winter's bias (0.63/0.91 m s^{-1}) and STD (2.07/2.04 m s^{-1}) values. Therefore, HSRL-2 wind speed error is higher for winter comparisons (0.63 m s^{-1} ± 2.07 m s^{-1}/0.91 m s^{-1} ± 2.04 m s^{-1}) than for summer comparisons (0.18 m s^{-1} ± 1.52 m s^{-1}/0.42 m s^{-1} ± 1.38 m s^{-1}). These results make sense because of the more turbulent and windy conditions in winter (i.e., relatively more wind speeds above 13.3 m s^{-1}), as discussed in Sect. 2.2, in contrast to summer months that coincide with a higher fraction of data representing wind speeds below 7 m s^{-1}. Despite the winter HSRL-2 wind speed retrievals having higher error than the summer ones, HSRL-2 wind speeds in the winter are still within ~0.9 m s^{-1} of the dropsonde wind speeds.

3.2 Case Studies

Wind speed data from two ACTIVATE research flights are analyzed (Research Flight 14 on 1 March 2020 and Research Flight 100 on 11 January 2022) to 1) demonstrate the special ability of the HSRL-2 to provide wind speed profiles that show the spatial variability of wind speed over time, which are beneficial to observe phenomena such as cloud evolution and sea-surface temperature dynamics and 2) identify potential drawbacks of using this retrieval method during days with high cloud fraction conditions. First, the 1 March 2020 case study is shown in Fig. 9 to address how HSRL-2 is beneficial for studying cloud and sea surface temperature dynamics.

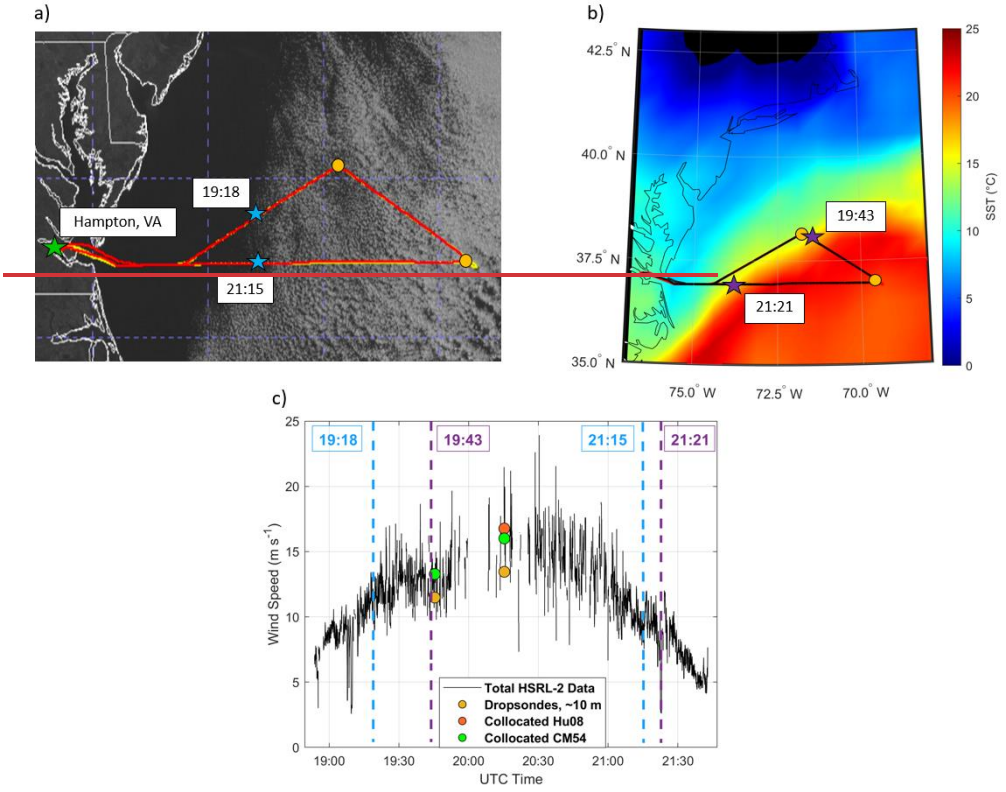

~~**Figure 9: a) Flight map of Falcon (yellow line), King Air (red line), and dropsondes (dark yellow circles) overlaid onto Geostationary Operational Environmental Satellite (GOES-16) cloud imagery for Research Flight 14 on 1 March 2020. Blue stars represent time stamps where the aircraft cross over from cloud-free to cloudy areas. b) Flight map overlaid onto map of MERRA-2 mean sea-surface temperature data (GMAO, 2015). Purple stars represent time stamps where the aircraft cross over sharp sea surface temperature changes associated with the Gulf Stream. c) Time series of wind speed data from HSRL-2 and dropsondes for the same flight, where lines signify total HSRL-2 wind speed data and circles indicate collocated wind speed data points used in analysis. Vertical lines represent time stamps of interest as indicated in a) and b). Collocated Hu08 and CM54 wind speed data points are on top of each other for the first pair of points in order of time.**~~

~~Included are the flight tracks overlaid on GOES imagery and sea surface temperature data from Modern-Era Retrospective Analysis for Research and Applications, Version 2 (MERRA-2) (Gelaro et al., 2017) (Fig. 9a-b). This flight and the associated morning flight on that same day have been the subject of several studies owing to its coincidence with cold air outbreak conditions (see cloud streets in Fig. 9a) and a flight strategy that allowed for detailed characterization of the evolving aerosol-cloud system as a function of distance offshore (Chen et al., 2022; Li et al., 2022; Tornow et al., 2022; Sorooshian et al., 2023).~~

Formatted: Font color: Black, Check spelling and grammar

There was a significant sea surface temperature gradient this day (Fig. 9b), which is common along the Gulf Stream border. The morning flight focused on a location with very detailed characterization including stacked level flight legs (i.e., termed a "wall") with the Falcon flying below, in, and above clouds with the King Air flying aloft to further characterize the same region. The afternoon flight consisted of both aircraft flying back to that same location, adjusting the sampling strategy to fly along the boundary layer wind direction in a quasi-Lagrangian fashion to keep studying the evolution of the air mass characterized in the morning. 4. ConclusionsThis case shows how the HSRL-2 samples in a broken-cloud field and provides a profile of how surface wind speeds spatially vary with time.

A special benefit of the HSRL-2 surface wind speed time series is the significant spatial gradient in surface wind speeds captured that otherwise would not be available solely with the dropsondes. The AVAPS dropsonde measurements provide data only at single points and cannot provide the spatial extent that the derived HSRL-2 surface wind speeds can contribute. Although the sharpest changes in the cloud field, sea surface temperature, and surface wind speed (Fig. 9) do not match exactly in space, surface wind speeds play an important role in the interplay between clouds, sea surface temperature, and MABL dynamics. This flight consisted of significantly higher wind speeds farther offshore, consistent with strong heat fluxes and postfrontal cloud development. Boundary layer wind speed and direction shear are key parameters relevant to understanding cloud formation, morphology, and life cycle during cold air outbreaks (e.g., Chen et al., 2022). In Fig. 9c, the two collocated wind data point pairs agreed within (in order of time) 1.80 m s^{-1} and 3.32 m s^{-1}; these agreements are less than what was observed in Fig. 3c. The agreement between HSRL-2 and dropsonde surface wind speeds is better at lower wind speeds as mentioned in Sect. 3.1, consistent with how the agreement for the first of the two pairs of collocated points in Fig. 3c was better as it was at lower wind speed.

It may be difficult to use HSRL-2 wind speed retrievals during days with high cloud fraction conditions. As mentioned in Sect. 3.1, there is poor agreement for wind speeds in the high wind regime relative to wind speeds in the low and intermediate

regimes. One source of these outliers comes from Research Flight 100 conducted on 11 January 2022 with the outliers being highlighted in Fig. 10.

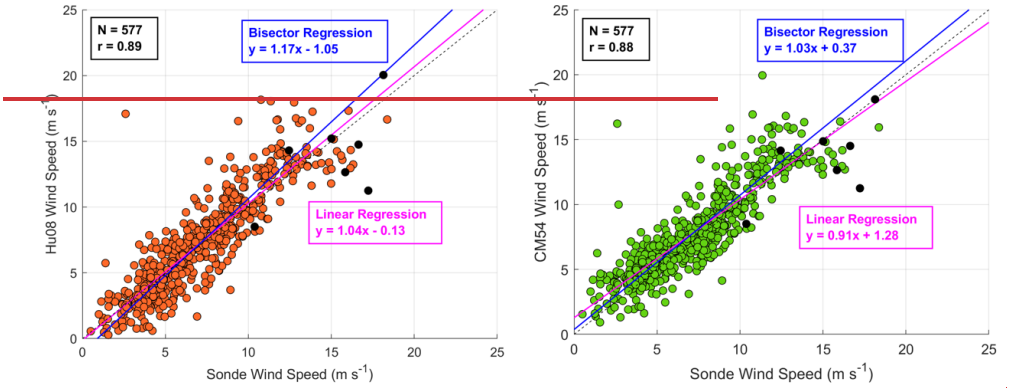

Figure 10: Hu08 and CM54 scatterplots from Fig. 4. with wind speed data points from 11 January 2022 highlighted using black circles.

Figure 10 shows that this research flight contributes to some of the largest outliers seen in Fig. 4. This day was deemed as an excellent cold air outbreak day due to significant temperature gradients at the air-sea interface, leading to a deep boundary layer, which strongly impacted the evolution of clouds on this day. Cloud coverage was significant (Fig. 11) along with visible steam fog and numerous whitecaps at the ocean surface. Precipitation and ice were also present, leading to icing on the aircraft instruments.

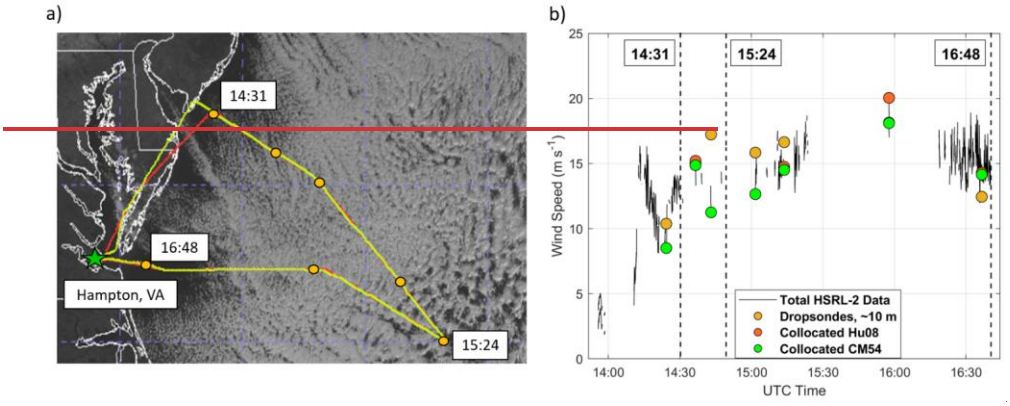

~~**Figure 11: a) Flight map of Falcon (yellow line), King Air (red line), and dropsondes (dark yellow circles) overlaid onto Geostationary Operational Environmental Satellite (GOES-16) cloud imagery for Research Flight 100 on 11 January 2022. Time stamps at 14:31 and 16:48 represent areas where HSRL-2 was able to retrieve wind speed data while the 15:24 time stamp shows where HSRL-2 had difficulty with wind speed retrievals. b) Time series of wind speed data from HSRL-2 and dropsondes for the same flight, where lines signify total HSRL-2 wind speed data and circles indicate collocated wind speed data points used in analysis. Vertical lines represent time stamps of interest as indicated in a). Some collocated Hu08 and CM54 wind speed points are on top of each other owing to similar values.**~~

~~As seen in Fig. 11b, most of the HSRL-2 wind speed data were missing during this flight due to quality control standards in the cloud screening of the data. If a wind speed retrieval is taken in an area with a high cloud fraction, which dominated most of the flight day (Fig. 11a), the retrieval is deemed a missing value. Therefore, it was more difficult to collocate dropsonde wind speeds with the Hu08 and CM54 wind speeds for a majority of the flight. The largest disagreement between HSRL-2 and dropsonde wind speeds is seen at 15:24 (Fig. 11b), occurring at an area with high cloud fraction and in turn had very limited HSRL-2 wind speed data that fit within the collocation criteria. The HSRL-2 had its most successful retrievals at 14:31 and 16:48 (Fig. 11a), which coincided with areas of less cloud cover. Although the HSRL-2 wind speed retrievals showed great success overall as seen in Sect. 3.1, this product is best used on days with cloud-free or broken cloud conditions.~~

~~4. Conclusions~~

This study introduces the High Spectral Resolution Lidar – generation 2 (HSRL-2) surface wind speed retrieval method, demonstrates its use, and evaluates its accuracy using NCAR AVAPS dropsonde data collected during the NASA ACTIVATE field campaign. ACTIVATE featured the joint deployment of the HSRL-2 and AVAPS dropsondes during six deployments from 2020 to 2022, enabling the accuracy of the HSRL-2 surface wind speed retrievals to be assessed using the coincident dropsonde measurements. Comparisons of HSRL-2 and dropsonde surface wind speeds show correlations of 0.89, slopes of 1.04 and 1.17, y-intercepts of -0.13 m s^{-1} and -1.05 m s^{-1} for linear and bisector regressions, respectively. The accuracy of the

HSRL-2 retrievals, as denoted by mean error, is calculated to be 0.15 m s^{-1} ± 1.80 m s^{-1}. It is also observed that the dropsonde surface wind speed measurements most closely match with the Hu et al. (2008) wind speed – wave-slope variance model than the Cox and Munk (1954) and Wu (1990) models for surface wind speeds below 7 m s^{-1}, which is an important finding because most ACTIVATE surface wind speeds fall into this category. After this overview of model performance, the HSRL-2 retrievals for surface wind speeds separated into below 7 m s^{-1} and between 7 m s^{-1} and 13.3 m s^{-1} categories are then evaluated in more detail. For surface wind speeds below 7 m s^{-1}, correlations of 0.66, slopes of 0.65 and 0.99, and y-intercepts of 1.10 m s^{-1} and -0.49 m s^{-1} are found and the accuracy of the retrievals is found to be -0.54 m s^{-1} ± 1.34 m s^{-1}. Surface wind speeds between 7 m s^{-1} and 13.3 m s^{-1} show correlations of 0.75, slopes of 0.64 and 0.85, and y-intercepts of 3.80 m s^{-1} and 1.87 m s^{-1} and the retrieval accuracy is shown to be 0.56 m s^{-1} ± 1.49 m s^{-1}. Statistics are not reported for surface wind speeds above 13.3 m s^{-1} because there are too few points in this category to make meaningful comparisons. These results showcase an important observation not seen in the cumulative results, which is that the HSRL-2 estimates surface wind speeds with a bias of ± ~0.5 m s^{-1} and an error of ± ~1.5 m s^{-1}. Lastly, the data are divided into winter and summer deployments (dates denoted in Sect. 2.1) to assess how the HSRL-2 performs between seasons. The winter surface wind speed data comparisons show correlations of 0.88, slopes of 0.95 and 1.08, and y-intercepts of 1.03 m s^{-1} and -0.08 m s^{-1} and the summer data show correlations of 0.87, slopes of 1.08 and 1.24, and y-intercepts of -0.69 m s^{-1} and -1.68 m s^{-1} (linear and bisector regressions, respectively). The accuracy of the lidar retrievals is reported as 0.63 m s^{-1} ± 2.07 m s^{-1} and -0.18 m s^{-1} ± 1.52 m s^{-1} for winter and summer, respectively. These findings show that HSRL-2 retrievals are more accurate in the summer than in winter, but still provide substantial (N = 236) and accurate surface wind speed data in winter as well.

~~This study introduces the High Spectral Resolution Lidar – generation 2 (HSRL-2) ocean surface wind speed retrieval method and demonstrates its use and accuracy using data collected during the NASA ACTIVATE field campaign from 2020 to 2022. Specifically, the capabilities of the HSRL-2 onboard the King Air are assessed by spatiotemporally collocating and comparing its data to NCAR AVAPS dropsonde measurements. This work presents the HSRL-2 retrieval algorithm using the Hu (Hu08) wind speed – wave-slope variance model with these results being compared with wind speeds using the well-known Cox-Munk (CM54) model. HSRL-2 wind speeds are strongly correlated with dropsonde wind speeds (r: 0.89/0.88) (Hu08/CM54) and these retrievals have an overall error of 0.15 m s^{-1} ± 1.80 m s^{-1} for Hu08 and 0.62 m s^{-1} ± 1.70 m s^{-1} for CM54. Results are also shown for wind speeds divided into low (Wind Speed < 7 m s^{-1}), intermediate (7 m s^{-1} ≤ Wind Speed < 13.3 m s^{-1}), and high (Wind Speed ≥ 13.3 m s^{-1}) categories. It is observed that high HSRL-2 winds have higher bias and variability compared to low HSRL-2 wind speeds. However, high HSRL-2 wind speeds are still within 2.20 m s^{-1} of the dropsonde wind speeds. Seasonal intercomparisons are also performed by categorizing the wind speed data into winter and summer deployment periods. The results of those comparisons indicate that HSRL-2 wind speeds in the winter have higher error (0.63 m s^{-1} ± 2.07 m s^{-1}/0.91 m s^{-1} ± 2.04 m s^{-1}) than in the summer (0.18 m s^{-1} ± 1.52 m s^{-1}/0.42 m s^{-1} ± 1.38 m s^{-1}), due in part to the winter having a higher frequency of wind speeds in the high wind speed regime whereas the summer contains more wind speeds in the low regime. Although the Hu08 results show a lower error, this study does not definitively conclude that either the Hu08 or CM54 model is better based on the statistics shown in Sect. 3.1.~~

This ~~novel~~ retrieval method offers a new path forward in airborne field work for the acquisition of ~~ocean~~ surface wind speed data at a high spatial (~75 m along track) and time (0.5 s) resolution~~, (10 s),~~ as demonstrated with two case study flights (Research Flight 29~~14~~ on 28 August~~1 March~~ 2020 and Research Flight ~~14~~14 on ~~1 March~~1 March 2020). The high horizontal spatial resolution of the HSRL-2 allows it to probe the fine-scale variability of surface wind speeds over time. As a result, the instrument provides near-continuous profiles of surface wind speeds over time that correspond to MABL phenomena such as SST dynamics and cloud evolution. Another important conclusion about the HSRL-2 surface retrievals is that the instrument can detect the surface in broken cloud scenes and are not limited to aerosol-free conditions like in Hu et al. (2008). Overall, having~~Having~~ such data can benefit model assimilation efforts and consequently several scientific applications related to air-sea interactions such as estimating heat fluxes, gas exchange, sea salt emissions and aerosol transport, and cloud life cycle. ~~However, another case study flight (Research Flight 100 on 11 January 2022) shows that the HSRL-2 wind speed retrievals are limited on days with high cloud fraction where the lidar signal is highly attenuated at the surface.~~

Forthcoming work will continue assessments of surface ~~surface~~ wind speed measurements during ACTIVATE by comparing dropsonde data to in situ measurements taken by the Turbulent Air Motion Measurement System (TAMMS) onboard the Falcon aircraft at its various altitude flight legs (between 120 m and 5 km) (Thornhill et al., 2003)~~. Comparisons will also be performed between TAMMS wind speeds and wind speed data from reanalysis models such as the Modern-Era Retrospective analysis for Research and Applications, version 2 (MERRA-2). Intercomparisons with MERRA-2 will be particularly important because this reanalysis model was used in NASA's Cloud-Aerosol Lidar and Pathfinder Satellite Observation (CALIPSO) retrievals of AOD using the surface scattering and modelled wind speed from MERRA-2.~~ Additional work is also warranted to assess the surface ~~surface~~ wind speed retrievals performed by ACTIVATE's other remote sensor, the Research Scanning Polarimeter (RSP), to fully demonstrate ACTIVATE's remote sensing capabilities.

Formatted: Font: +Body (Times New Roman), Font color: Text 1

Data Availability

ACTIVATE airborne data are available through https://asdc.larc.nasa.gov/project/ACTIVATE (ACTIVATE Science Team, 2020). MERRA-2 mean sea surface temperature data are taken from the 2d, 1-Hourly, Time-Averaged, Single-Level, Assimilation, Surface Flux Diagnostics V5.12.4 (M2T1NXFLX) product found at https://disc.gsfc.nasa.gov/datasets/M2T1NXFLX_5.12.4/summary (doi.org/10.5067/7MCPBJ41Y0K6). GOES-16 data are from https://asdc.larc.nasa.gov/ACTIVATE/ACTIVATE-Satellite_1 (doi: 10.5067/ASDC/SUBORBITAL/ACTIVATE-Satellite_1).

Author Contribution

SD performed all analyses with input from all co-authors. SD, JH, RF, CH, JR, and AS prepared manuscript with all co-authors involved in review/editing. TS, DH, SS, and CR conducted flight scientist duties on the King Air and helped with preparation and deployment of dropsondes. JH, RF, MF, CH, BC, DH, SS, TS, and EC were responsible for the HSRL-2 instrumentation and KT, CR, and HV were responsible for the NCAR AVAPS dropsonde instrumentation collected and subsequent archival of surface ~~surface~~ wind speed data sets needed to conduct this analysis. JH, JR, YH, RF, CH, and BC all contributed with formulation of HSRL-2 retrieval algorithm.

Competing Interests

The authors declare that they have no conflict of interest.

Disclaimer

Publisher's note: Copernicus Publications remains neutral with regard to jurisdictional claims in published maps and institutional affiliations.

Acknowledgements

The work was funded by ACTIVATE, a NASA Earth Venture Suborbital-3 (EVS-3) investigation funded by NASA's Earth Science Division and managed through the Earth System Science Pathfinder Program Office. We thank pilots and aircraft maintenance personnel of NASA Langley Research Services Directorate for successfully conducting ACTIVATE flights. The MERRA-2 1-Hourly, Time-Averaged, Single-Level, Assimilation, Surface Flux Diagnostics V5.12.4 (M2T1NXFLX) data used in this effort were acquired as part of the activities of NASA's Science Mission Directorate and are archived and distributed by the Goddard Earth Sciences (GES) Data and Information Services Center (DISC).

Financial support

University of Arizona investigators were funded by NASA grant no. 80NSSC19K0442.

References

ACTIVATE Science Team: Aerosol Cloud meTeorology Interactions oVer the western ATlantic Experiment Data [dataset], doi.org/10.5067/SUBORBITAL/ACTIVATE/DATA001, 2020.

Aldhaif, A. M., Lopez, D. H., Dadashazar, H., and Sorooshian, A.: Sources, frequency, and chemical nature of dust events impacting the United States East Coast, Atmospheric Environment, 231, 117456, https://doi.org/10.1016/j.atmosenv.2020.117456, 2020.

Bedka, K. M., Nehrir, A. R., Kavaya, M., Barton-Grimley, R., Beaubien, M., Carroll, B., Collins, J., Cooney, J., Emmitt, G. D., Greco, S., Kooi, S., Lee, T., Liu, Z., Rodier, S., and Skofronick-Jackson, G.: Airborne lidar observations of wind, water vapor, and aerosol profiles during the NASA Aeolus calibration and validation (Cal/Val) test flight campaign, Atmos. Meas. Tech., 14, 4305-4334, 10.5194/amt-14-4305-2021, 2021.

Bellouin, N., Quaas, J., Gryspeerdt, E., Kinne, S., Stier, P., Watson-Parris, D., Boucher, O., Carslaw, K. S., Christensen, M., Daniau, A.-L., Dufresne, J.-L., Feingold, G., Fiedler, S., Forster, P., Gettelman, A., Haywood, J. M., Lohmann, U., Malavelle, F., Mauritsen, T., McCoy, D. T., Myhre, G., Mülmenstädt, J., Neubauer, D., Possner, A., Rugenstein, M., Sato, Y., Schulz, M., Schwartz, S. E., Sourdeval, O., Storelvmo, T., Toll, V., Winker, D., and Stevens, B.: Bounding Global Aerosol Radiative Forcing of Climate Change, Reviews of Geophysics, 58, e2019RG000660, https://doi.org/10.1029/2019RG000660, 2020.

Brunke, M. A., Cutler, L., Urzua, R. D., Corral, A. F., Crosbie, E., Hair, J., Hostetler, C., Kirschler, S., Larson, V., Li, X.-Y., Ma, P.-L., Minke, A., Moore, R., Robinson, C. E., Scarino, A. J., Schlosser, J., Shook, M., Sorooshian, A., Lee Thornhill, K., Voigt, C., Wan, H., Wang, H., Winstead, E., Zeng, X., Zhang, S., and Ziemba, L. D.: Aircraft Observations of Turbulence in Cloudy and Cloud-Free Boundary Layers Over the Western North Atlantic Ocean From ACTIVATE and Implications for the Earth System Model Evaluation and Development, Journal of Geophysical Research: Atmospheres, 127, e2022JD036480, https://doi.org/10.1029/2022JD036480, 2022.

Burton, S. P., Ferrare, R. A., Hostetler, C. A., Hair, J. W., Rogers, R. R., Obland, M. D., Butler, C. F., Cook, A. L., Harper, D. B., and Froyd, K. D.: Aerosol classification using airborne High Spectral Resolution Lidar measurements – methodology and examples, Atmos. Meas. Tech., 5, 73-98, 10.5194/amt-5-73-2012, 2012.

Burton, S. P., Hostetler, C. A., Cook, A. L., Hair, J. W., Seaman, S. T., Scola, S., Harper, D. B., Smith, J. A., Fenn, M. A., Ferrare, R. A., Saide, P. E., Chemyakin, E. V., and Müller, D.: Calibration of a high spectral resolution lidar using a Michelson interferometer, with data examples from ORACLES, Appl. Opt., 57, 6061-6075, 10.1364/AO.57.006061, 2018.

Carvalho, D.: An Assessment of NASA's GMAO MERRA-2 Reanalysis Surface Winds, Journal of Climate, 32, 8261-8281, https://doi.org/10.1175/JCLI-D-19-0199.1, 2019.

Chemyakin, E., Stamnes, S., Hair, J., Burton, S. P., Bell, A., Hostetler, C., Ferrare, R., Chowdhary, J., Moore, R., Ziemba, L., Crosbie, E., Robinson, C., Shook, M., Thornhill, L., Winstead, E., Hu, Y., van Diedenhoven, B., and Cairns, B.: Efficient single-scattering look-up table for lidar and polarimeter water cloud studies, Opt. Lett., 48, 13-16, 10.1364/OL.474282, 2023.

Chen, J., Wang, H., Li, X., Painemal, D., Sorooshian, A., Thornhill, K. L., Robinson, C., and Shingler, T.: Impact of Meteorological Factors on the Mesoscale Morphology of Cloud Streets during a Cold-Air Outbreak over the Western North Atlantic, Journal of the Atmospheric Sciences, 79, 2863-2879, https://doi.org/10.1175/JAS-D-22-0034.1, 2022.

Christoudias, T., Pozzer, A., and Lelieveld, J.: Influence of the North Atlantic Oscillation on air pollution transport, Atmos. Chem. Phys., 12, 869-877, 10.5194/acp-12-869-2012, 2012.

Corral, A. F., Choi, Y., Crosbie, E., Dadashazar, H., DiGangi, J. P., Diskin, G. S., Fenn, M., Harper, D. B., Kirschler, S., Liu, H., Moore, R. H., Nowak, J. B., Scarino, A. J., Seaman, S., Shingler, T., Shook, M. A., Thornhill, K. L., Voigt, C., Zhang, B., Ziemba, L. D., and Sorooshian, A.: Cold Air Outbreaks Promote New Particle Formation Off the U.S. East Coast, Geophysical Research Letters, 49, e2021GL096073, https://doi.org/10.1029/2021GL096073, 2022.

Cox, C. and Munk, W.: Measurement of the Roughness of the Sea Surface from Photographs of the Sun's Glitter, J. Opt. Soc. Am., 44, 838-850, 10.1364/JOSA.44.000838, 1954.

Creilson, J. K., Fishman, J., and Wozniak, A. E.: Intercontinental transport of tropospheric ozone: a study of its seasonal variability across the North Atlantic utilizing tropospheric ozone residuals and its relationship to the North Atlantic Oscillation, Atmos. Chem. Phys., 3, 2053-2066, 10.5194/acp-3-2053-2003, 2003.

Dadashazar, H., Painemal, D., Alipanah, M., Brunke, M., Chellappan, S., Corral, A. F., Crosbie, E., Kirschler, S., Liu, H., Moore, R. H., Robinson, C., Scarino, A. J., Shook, M., Sinclair, K., Thornhill, K. L., Voigt, C., Wang, H., Winstead, E., Zeng, X., Ziemba, L., Zuidema, P., and Sorooshian, A.: Cloud drop number concentrations over the western North Atlantic Ocean: seasonal cycle, aerosol interrelationships, and other influential factors, Atmos. Chem. Phys., 21, 10499-10526, 10.5194/acp-21-10499-2021, 2021.

Dierssen, H. M.: Hyperspectral Measurements, Parameterizations, and Atmospheric Correction of Whitecaps and Foam From Visible to Shortwave Infrared for Ocean Color Remote Sensing, Frontiers in Earth Science, 7, 10.3389/feart.2019.00014, 2019.

Ferrare, R., Hair, J., Hostetler, C., Shingler, T., Burton, S. P., Fenn, M., Clayton, M., Scarino, A. J., Harper, D., Seaman, S., Cook, A., Crosbie, E., Winstead, E., Ziemba, L., Thornhill, L., Robinson, C., Moore, R., Vaughan, M., Sorooshian, A., Schlosser, J. S., Liu, H., Zhang, B., Diskin, G., DiGangi, J., Nowak, J., Choi, Y., Zuidema, P., and Chellappan, S.: Airborne HSRL-2 measurements of elevated aerosol depolarization associated with non-spherical sea salt, Frontiers in Remote Sensing, 4, 10.3389/frsen.2023.1143944, 2023.

Gelaro, R., McCarty, W., Suárez, M. J., Todling, R., Molod, A., Takacs, L., Randles, C. A., Darmenov, A., Bosilovich, M. G., Reichle, R., Wargan, K., Coy, L., Cullather, R., Draper, C., Akella, S., Buchard, V., Conaty, A., da Silva, A. M., Gu, W., Kim,

G.-K., Koster, R., Lucchesi, R., Merkova, D., Nielsen, J. E., Partyka, G., Pawson, S., Putman, W., Rienecker, M., Schubert, S. D., Sienkiewicz, M., and Zhao, B.: The Modern-Era Retrospective Analysis for Research and Applications, Version 2 (MERRA-2), Journal of Climate, 30, 5419-5454, https://doi.org/10.1175/JCLI-D-16-0758.1, 2017.

GMAO: MERRA-2 tavg1_2d_flx_Nx: 2d, 1-Hourly, Time-Averaged, Single-Level, Assimilation, Surface Flux Diagnostics V5.12.4 [dataset], 2015.

Gordon, H. R. and Wang, M.: Influence of oceanic whitecaps on atmospheric correction of ocean-color sensors, Appl. Opt., 33, 7754-7763, 10.1364/AO.33.007754, 1994.

Hair, J. W., Hostetler, C. A., Cook, A. L., Harper, D. B., Ferrare, R. A., Mack, T. L., Welch, W., Izquierdo, L. R., and Hovis, F. E.: Airborne High Spectral Resolution Lidar for profiling aerosol optical properties, Appl. Opt., 47, 6734-6752, 10.1364/AO.47.006734, 2008.

Hu, Y., Stamnes, K., Vaughan, M., Pelon, J., Weimer, C., Wu, D., Cisewski, M., Sun, W., Yang, P., Lin, B., Omar, A., Flittner, D., Hostetler, C., Trepte, C., Winker, D., Gibson, G., and Santa-Maria, M.: Sea surface wind speed estimation from space-based lidar measurements, Atmos. Chem. Phys., 8, 3593-3601, 10.5194/acp-8-3593-2008, 2008.

Josset, D., Pelon, J., and Hu, Y.: Multi-Instrument Calibration Method Based on a Multiwavelength Ocean Surface Model, IEEE Geoscience and Remote Sensing Letters, 7, 195-199, 10.1109/LGRS.2009.2030906, 2010a.

Josset, D., Pelon, J., Protat, A., and Flamant, C.: New approach to determine aerosol optical depth from combined CALIPSO and CloudSat ocean surface echoes, Geophysical Research Letters, 35, https://doi.org/10.1029/2008GL033442, 2008.

Josset, D., Zhai, P.-W., Hu, Y., Pelon, J., and Lucker, P. L.: Lidar equation for ocean surface and subsurface, Opt. Express, 18, 20862-20875, 10.1364/OE.18.020862, 2010b.

Kiliyanpilakkil, V. P. and Meskhidze, N.: Deriving the effect of wind speed on clean marine aerosol optical properties using the A-Train satellites, Atmos. Chem. Phys., 11, 11401-11413, 10.5194/acp-11-11401-2011, 2011.

Kirschler, S., Voigt, C., Anderson, B., Campos Braga, R., Chen, G., Corral, A. F., Crosbie, E., Dadashazar, H., Ferrare, R. A., Hahn, V., Hendricks, J., Kaufmann, S., Moore, R., Pöhlker, M. L., Robinson, C., Scarino, A. J., Schollmayer, D., Shook, M. A., Thornhill, K. L., Winstead, E., Ziemba, L. D., and Sorooshian, A.: Seasonal updraft speeds change cloud droplet number concentrations in low-level clouds over the western North Atlantic, Atmos. Chem. Phys., 22, 8299-8319, 10.5194/acp-22-8299-2022, 2022.

Koepke, P.: Effective reflectance of oceanic whitecaps, Appl. Opt., 23, 1816-1824, 10.1364/AO.23.001816, 1984.

Lamb, P. J. and Peppler, R. A.: North Atlantic Oscillation: Concept and an Application, Bulletin of the American Meteorological Society, 68, 1218-1225, https://doi.org/10.1175/1520-0477(1987)068<1218:NAOCAA>2.0.CO;2, 1987.

Li, Q., Jacob, D. J., Bey, I., Palmer, P. I., Duncan, B. N., Field, B. D., Martin, R. V., Fiore, A. M., Yantosca, R. M., Parrish, D. D., Simmonds, P. G., and Oltmans, S. J.: Transatlantic transport of pollution and its effects on surface ozone in Europe and North America, Journal of Geophysical Research: Atmospheres, 107, ACH 4-1-ACH 4-21, https://doi.org/10.1029/2001JD001422, 2002.

Li, X.-Y., Wang, H., Chen, J., Endo, S., George, G., Cairns, B., Chellappan, S., Zeng, X., Kirschler, S., Voigt, C., Sorooshian, A., Crosbie, E., Chen, G., Ferrare, R. A., Gustafson, W. I., Hair, J. W., Kleb, M. M., Liu, H., Moore, R., Painemal, D., Robinson, C., Scarino, A. J., Shook, M., Shingler, T. J., Thornhill, K. L., Tornow, F., Xiao, H., Ziemba, L. D., and Zuidema, P.: Large-Eddy Simulations of Marine Boundary Layer Clouds Associated with Cold-Air Outbreaks during the ACTIVATE Campaign. Part I: Case Setup and Sensitivities to Large-Scale Forcings, Journal of the Atmospheric Sciences, 79, 73-100, https://doi.org/10.1175/JAS-D-21-0123.1, 2022.

Mardi, A. H., Dadashazar, H., Painemal, D., Shingler, T., Seaman, S. T., Fenn, M. A., Hostetler, C. A., and Sorooshian, A.: Biomass Burning Over the United States East Coast and Western North Atlantic Ocean: Implications for Clouds and Air Quality, Journal of Geophysical Research: Atmospheres, 126, e2021JD034916, https://doi.org/10.1029/2021JD034916, 2021.

Martin, C. and Suhr, I.: NCAR/EOL Atmospheric Sounding Processing ENvironment (ASPEN) software. Version 3.4.5. [dataset], 2021.

Moore, K. D., Voss, K. J., and Gordon, H. R.: Spectral reflectance of whitecaps: Their contribution to water-leaving radiance, Journal of Geophysical Research: Oceans, 105, 6493-6499, https://doi.org/10.1029/1999JC900334, 2000.

Murphy, A. and Hu, Y.: Retrieving Aerosol Optical Depth and High Spatial Resolution Ocean Surface Wind Speed From CALIPSO: A Neural Network Approach, Frontiers in Remote Sensing, 1, 10.3389/frsen.2020.614029, 2021.

Nair, A. K. M. and Rajeev, K.: Multiyear CloudSat and CALIPSO Observations of the Dependence of Cloud Vertical Distribution on Sea Surface Temperature and Tropospheric Dynamics, Journal of Climate, 27, 672-683, https://doi.org/10.1175/JCLI-D-13-00062.1, 2014.

Neukermans, G., Harmel, T., Galí, M., Rudorff, N., Chowdhary, J., Dubovik, O., Hostetler, C., Hu, Y., Jamet, C., Knobelspiesse, K., Lehahn, Y., Litvinov, P., Sayer, A. M., Ward, B., Boss, E., Koren, I., and Miller, L. A.: Harnessing remote sensing to address critical science questions on ocean-atmosphere interactions, Elementa: Science of the Anthropocene, 6, 10.1525/elementa.331, 2018.

Painemal, D., Corral, A. F., Sorooshian, A., Brunke, M. A., Chellappan, S., Afzali Gorooh, V., Ham, S.-H., O'Neill, L., Smith Jr., W. L., Tselioudis, G., Wang, H., Zeng, X., and Zuidema, P.: An Overview of Atmospheric Features Over the Western North Atlantic Ocean and North American East Coast—Part 2: Circulation, Boundary Layer, and Clouds, Journal of Geophysical Research: Atmospheres, 126, e2020JD033423, https://doi.org/10.1029/2020JD033423, 2021.

Painemal, D., Chellappan, S., Smith Jr., W. L., Spangenberg, D., Park, J. M., Ackerman, A., Chen, J., Crosbie, E., Ferrare, R., Hair, J., Kirschler, S., Li, X.-Y., McComiskey, A., Moore, R. H., Sanchez, K., Sorooshian, A., Tornow, F., Voigt, C., Wang, H., Winstead, E., Zeng, X., Ziemba, L., and Zuidema, P.: Wintertime Synoptic Patterns of Midlatitude Boundary Layer Clouds Over the Western North Atlantic: Climatology and Insights From In Situ ACTIVATE Observations, Journal of Geophysical Research: Atmospheres, 128, e2022JD037725, https://doi.org/10.1029/2022JD037725, 2023.

Paiva, V., Kampel, M., and Camayo, R.: Comparison of Multiple Surface Ocean Wind Products with Buoy Data over Blue Amazon (Brazilian Continental Margin), Advances in Meteorology, 2021, 6680626, 10.1155/2021/6680626, 2021.

Ricker, W. E.: Linear Regressions in Fishery Research, Journal of the Fisheries Research Board of Canada, 30, 409-434, 10.1139/f73-072, 1973.

Scarino, A. J., Obland, M. D., Fast, J. D., Burton, S. P., Ferrare, R. A., Hostetler, C. A., Berg, L. K., Lefer, B., Haman, C., Hair, J. W., Rogers, R. R., Butler, C., Cook, A. L., and Harper, D. B.: Comparison of mixed layer heights from airborne high spectral resolution lidar, ground-based measurements, and the WRF-Chem model during CalNex and CARES, Atmos. Chem. Phys., 14, 5547-5560, 10.5194/acp-14-5547-2014, 2014.

Schlosser, J. S., Stamnes, S., Burton, S. P., Cairns, B., Crosbie, E., Van Diedenhoven, B., Diskin, G., Dmitrovic, S., Ferrare, R., Hair, J. W., Hostetler, C. A., Hu, Y., Liu, X., Moore, R. H., Shingler, T., Shook, M. A., Thornhill, K. L., Winstead, E., Ziemba, L., and Sorooshian, A.: Polarimeter + Lidar–Derived Aerosol Particle Number Concentration, Frontiers in Remote Sensing, 3, 10.3389/frsen.2022.885332, 2022.

Schulien, J. A., Behrenfeld, M. J., Hair, J. W., Hostetler, C. A., and Twardowski, M. S.: Vertically- resolved phytoplankton carbon and net primary production from a high spectral resolution lidar, Opt. Express, 25, 13577-13587, 10.1364/OE.25.013577, 2017.

Seethala, C., Zuidema, P., Edson, J., Brunke, M., Chen, G., Li, X.-Y., Painemal, D., Robinson, C., Shingler, T., Shook, M., Sorooshian, A., Thornhill, L., Tornow, F., Wang, H., Zeng, X., and Ziemba, L.: On Assessing ERA5 and MERRA2 Representations of Cold-Air Outbreaks Across the Gulf Stream, Geophysical Research Letters, 48, e2021GL094364, https://doi.org/10.1029/2021GL094364, 2021.

Sorooshian, A., Corral, A. F., Braun, R. A., Cairns, B., Crosbie, E., Ferrare, R., Hair, J., Kleb, M. M., Hossein Mardi, A., Maring, H., McComiskey, A., Moore, R., Painemal, D., Scarino, A. J., Schlosser, J., Shingler, T., Shook, M., Wang, H., Zeng, X., Ziemba, L., and Zuidema, P.: Atmospheric Research Over the Western North Atlantic Ocean Region and North American East Coast: A Review of Past Work and Challenges Ahead, Journal of Geophysical Research: Atmospheres, 125, e2019JD031626, https://doi.org/10.1029/2019JD031626, 2020.

Sorooshian, A., Anderson, B., Bauer, S. E., Braun, R. A., Cairns, B., Crosbie, E., Dadashazar, H., Diskin, G., Ferrare, R., Flagan, R. C., Hair, J., Hostetler, C., Jonsson, H. H., Kleb, M. M., Liu, H., MacDonald, A. B., McComiskey, A., Moore, R., Painemal, D., Russell, L. M., Seinfeld, J. H., Shook, M., Smith, W. L., Thornhill, K., Tselioudis, G., Wang, H., Zeng, X., Zhang, B., Ziemba, L., and Zuidema, P.: Aerosol–Cloud–Meteorology Interaction Airborne Field Investigations: Using Lessons Learned from the U.S. West Coast in the Design of ACTIVATE off the U.S. East Coast, Bulletin of the American Meteorological Society, 100, 1511-1528, https://doi.org/10.1175/BAMS-D-18-0100.1, 2019.

Sorooshian, A., Alexandrov, M. D., Bell, A. D., Bennett, R., Betito, G., Burton, S. P., Buzanowicz, M. E., Cairns, B., Chemyakin, E. V., Chen, G., Choi, Y., Collister, B. L., Cook, A. L., Corral, A. F., Crosbie, E. C., van Diedenhoven, B., DiGangi, J. P., Diskin, G. S., Dmitrovic, S., Edwards, E. L., Fenn, M. A., Ferrare, R. A., van Gilst, D., Hair, J. W., Harper, D. B., Hilario, M. R. A., Hostetler, C. A., Jester, N., Jones, M., Kirschler, S., Kleb, M. M., Kusterer, J. M., Leavor, S., Lee, J. W., Liu, H., McCauley, K., Moore, R. H., Nied, J., Notari, A., Nowak, J. B., Painemal, D., Phillips, K. E., Robinson, C. E., Scarino, A. J., Schlosser, J. S., Seaman, S. T., Seethala, C., Shingler, T. J., Shook, M. A., Sinclair, K. A., Smith Jr, W. L., Spangenberg, D. A., Stamnes, S. A., Thornhill, K. L., Voigt, C., Vömel, H., Wasilewski, A. P., Wang, H., Winstead, E. L., Zeider, K., Zeng, X., Zhang, B., Ziemba, L. D., and Zuidema, P.: Spatially-coordinated airborne data and complementary products for aerosol, gas, cloud, and meteorological studies: The NASA ACTIVATE dataset, Earth Syst. Sci. Data Discuss., 2023, 1-79, 10.5194/essd-2023-109, 2023.

Sun, K., Dai, G., Wu, S., Reitebuch, O., Baars, H., Liu, J., and Zhang, S.: Correlation between marine aerosol optical properties and wind fields over remote oceans with use of spaceborne lidar observations, EGUsphere, 2023, 1-34, 10.5194/egusphere-2023-433, 2023.

Thornhill, K. L., Anderson, B. E., Barrick, J. D. W., Bagwell, D. R., Friesen, R., and Lenschow, D. H.: Air motion intercomparison flights during Transport and Chemical Evolution in the Pacific (TRACE-P)/ACE-ASIA, Journal of Geophysical Research: Atmospheres, 108, https://doi.org/10.1029/2002JD003108, 2003.

Tornow, F., Ackerman, A. S., Fridlind, A. M., Cairns, B., Crosbie, E. C., Kirschler, S., Moore, R. H., Painemal, D., Robinson, C. E., Seethala, C., Shook, M. A., Voigt, C., Winstead, E. L., Ziemba, L. D., Zuidema, P., and Sorooshian, A.: Dilution of

Boundary Layer Cloud Condensation Nucleus Concentrations by Free Tropospheric Entrainment During Marine Cold Air Outbreaks, Geophysical Research Letters, 49, e2022GL098444, https://doi.org/10.1029/2022GL098444, 2022.

van Diedenhoven, B., Hasekamp, O. P., Cairns, B., Schuster, G. L., Stammes, S., Shook, M. A., and Ziemba, L. D.: Remote sensing of aerosol water fraction, dry size distribution and soluble fraction using multi-angle, multi-spectral polarimetry, EGUsphere, 2022, 1-41, 10.5194/egusphere-2022-670, 2022.

Venkata, S. L. and Reagan, J. A.: Aerosol Retrievals from CALIPSO Lidar Ocean Surface Returns, Remote Sensing, 8, 1006, 2016.

Vömel, H. and Dunion, J.: Chapter 10 - Aircraft dropsonde campaigns, in: Field Measurements for Passive Environmental Remote Sensing, edited by: Nalli, N. R., Elsevier, 185-194, https://doi.org/10.1016/B978-0-12-823953-7.00021-6, 2023.

Vömel, H., Goodstein, M., Tudor, L., Witte, J., Fuchs-Stone, Ž., Sentić, S., Raymond, D., Martinez-Claros, J., Juračić, A., Maithel, V., and Whitaker, J. W.: High-resolution in situ observations of atmospheric thermodynamics using dropsondes during the Organization of Tropical East Pacific Convection (OTREC) field campaign, Earth Syst. Sci. Data, 13, 1107-1117, 10.5194/essd-13-1107-2021, 2021.

Whitlock, C. H., Bartlett, D. S., and Gurganus, E. A.: Sea foam reflectance and influence on optimum wavelength for remote sensing of ocean aerosols, Geophysical Research Letters, 9, 719-722, 1982.

Wu, C. and Yu, J. Z.: Evaluation of linear regression techniques for atmospheric applications: the importance of appropriate weighting, Atmos. Meas. Tech., 11, 1233-1250, 10.5194/amt-11-1233-2018, 2018.

Wu, J.: Mean square slopes of the wind-disturbed water surface, their magnitude, directionality, and composition, Radio Science, 25, 37-48, https://doi.org/10.1029/RS025i001p00037, 1990.